In vivo multiscale measurements of solid stresses in tumors reveal scale-dependent stress transmission

Sue Zhang[1], Gabrielle Grifno[1], Rachel Passaro[1], Kathryn Regan[1], Siyi Zheng[1], Muhamed Hadzipasic[1,3], Rohin Banerji[1], Logan O'Connor[1], Vinson Chu[1], Sung Yeon Kim[1], Jiarui Yang[1], Linzheng Shi[1], Kavon Karrobi[1], Darren Roblyer[1], Mark W. Grinstaff[1,2], Hadi T. Nia[1,*]

[1]Department of Biomedical Engineering, Boston University, Boston, MA
[2]Department of Chemistry, Boston University, Boston, MA
[3]Department of Neurosurgery, Massachusetts General Hospital, Boston, MA

*Corresponding author: Hadi T. Nia, htnia@bu.edu

Solid stress, one of the physical hallmarks of cancer, affects trafficking and infiltration of immune cells, promotes metastasis and tumorigenic pathways, and impedes therapeutic delivery. Despite these clinical ramifications, questions remain regarding the origins and consequences of solid stresses. Answering these fundamental questions requires probing solid stresses at the cellular scale, where biological and immunological responses manifest, as well as *in vivo*, where the complexities of the tumor microenvironment exist. Here, we report the first *in vivo* and multi-scale optical measurements of solid stress in mouse models of breast cancer using multi-modal intravital microscopy of deformable hydrogels in tumors complemented with mathematical modeling. Utilizing the capabilities of these methods, such as the high-resolution, longitudinal, and 3-D measurements of local solid stress, we measure and compare solid stresses (i) at the single cell vs tissue scale, (ii) in primary vs metastatic tumors, (iii) *in vivo* vs *in vitro* settings, and (iv) *in vivo* vs post-mortem. In primary tumors, we find that solid stress transmission is scale-dependent, as tumor cells experience significantly lower stress in comparison to stress measured at the tissue scale, implying the presence of potential biophysical mechanisms that tumor cells utilize to protect themselves against lethally high solid stresses. Further, we find that cancer cells in lung metastasis experience significantly higher level of solid stresses compared to primary tumors from the same cancer cells, implying the role of the tumor microenvironment on genesis of solid stresses. These insights into the scale- and microenvironment-dependence of solid stress will further inform the discovery of new therapeutic strategies that sensitize cancer cells to solid stresses to induce cell death.

Solid stress, defined as the mechanical force generated and transmitted by the solid components of a tumor, is a newly identified physical hallmark of cancer with crucial consequences for tumor progression and treatment response[1]. Cells sense solid stresses directly and indirectly via mechanosensitive interactions such as cell-extracellular matrix (ECM) and cell-cell adhesions[2-5], activation of tensile-responsive ECM proteins[6-8], and nuclear deformation[9,10]. Solid stress causes the compression of blood and lymphatic vessels[1,11-14] which contributes to hypoxia[11,13] and impedes drug delivery[15,16], affects T-cell trafficking and infiltration[17], promotes invasiveness of cancer cells[18,19], stimulates tumorigenic pathways[20], and induces neuronal damage[21,22]. Targeting solid stress, when combined with standard-of-care anti-cancer treatments, prolongs survival in preclinical studies[11,14,23-25] and is currently being evaluated in clinical trials[26] with promising outcomes[27]. While some of the pathophysiological consequences of solid stresses in tumors are now better known, the direct cellular responses to solid stresses and the molecular pathways that are directly activated by them are not fully understood. This is due mainly to a lack of appropriate tools to measure the solid stresses that individual single cancer cells experience *in vivo*, where the complexities of tumor microenvironment exist.

Despite the recent progress in measuring solid stresses in cancer *ex vivo*[21,22,28-30] and *in vitro*[31-33] the measurement of *in vivo* solid stress at multiple scales in tumors is an unmet need. In addition, the existing methods to measure solid stresses in murine and human tumors[21,22,28,29,34-36] are at the tissue scale and lack the spatial resolution to measure the stresses that individual tumor cells experience. These existing methods are also invasive, typically performed at terminal points, and lack the capabilities for longitudinal monitoring of solid stresses. Furthermore, the existing methods are limited to reporting 1-D and 2-D profiles of solid stresses[28,29] and do not provide the 3-D distribution of solid stress as a tensor, which is necessary to describe the anisotropy and heterogeneities of stresses. Therefore, it is critical to develop a method to non-invasively

monitor *in vivo* solid stresses at high spatiotemporal resolution across the length scales from the cellular to the tissue scale would allow deeper insight into the origins and consequences of solid stresses.

Our previous methods report that solid stresses measured at the macroscale in tumors result in up to 20% strain (deformation) after partial stress relaxation[28,29], reflecting extremely high stresses in the tumors that are lethal to cells[37-39] and in the normal surrounding tissue[21]. These observations raised the following open questions that motivate our current study to measure solid stresses at the cellular level: How can tumor cells survive under such high solid stresses? Are there any biological and/or physical mechanisms that tumor cells utilize to protect themselves from lethally high solid stresses? Recently proposed biological mechanisms to protect tumor cells against high levels of solid stress include the loss of p53[5,37] and use of osmotic regulation[40] to enable neoplastic cells to survive under high mechanical stress. Here, we show that, in addition to biological mechanisms, potential biophysical mechanisms may dissipate the large tissue-level stresses and protect tumor cells against high level of solid stresses.

Here, we describe the first *in vivo* and multi-scale optical measurements of solid stress in tumors using intravital imaging of deformable hydrogel spheres embedded within primary tumors or in lung metastatic tumors through the hematogenous route. Our method utilizes multimodal intravital microscopy to obtain 3-D high-resolution spatial and longitudinal measurement of solid stresses *in vivo*. We compared the solid stresses in primary breast tumors vs breast cancer lung metastasis and found that solid stresses are significantly higher in metastatic settings, although both metastatic and primary tumors were induced from the same cancer cells. Our results demonstrate the role of microenvironment on solid stress genesis and a potential implication on the differential treatment response between primary and metastatic settings. Furthermore, our method enables the comparison between the *in vitro* and *in vivo* models of solid stresses to evaluate how closely these *in vitro* models recapitulate the physical tumor microenvironment. While it has been shown through mathematical modeling that stress transmission is scale dependent[41-43], we reveal for the first time experimentally that solid stress transmission is scale dependent. Interestingly, we find that the stresses that individual tumor cells experience is a factor of 5-8 lower than the large stress levels measured at the tissue scales. This finding lays the groundwork for discovering novel biophysical mechanisms that cancer cells utilize to evade cell death from high mechanical stresses, and for establishing new therapeutic strategies aimed at increasing the vulnerability of cancer cells to mechanical stresses, resulting in cancer cell death.

Development of an *in vivo* solid stress measurement system for primary and metastatic tumors

To measure solid stress *in vivo*, we employed intravital imaging of spherical polyacrylamide (PA) beads as solid stress sensors. PA beads are biocompatible, deformable, tunable in size and Young's modulus, and amenable to core and surface functionalization, including the covalent attachment of a fluorophore[44]. We fabricated fluorescently-labelled PA beads using an inverse emulsion polymerization, as previously reported[31,33,45] and filtered them for the desired size ranges using micron-sized meshes. After sterilization by UV light, PA beads were functionalized with fibronectin to mimic cell-matrix interactions between the PA beads and surrounding tissue and to promote uptake of PA beads into murine tumors (Fig. 1a). PA beads were fabricated for measurements at the tissue-scale (397 ± 69 μm in diameter) or cellular-scale (28.7 ± 18.2 μm) to investigate the scale-dependence of solid stress across an order of magnitude change in length scale (Fig. 1b). We implemented two syngeneic models of breast cancer, MCa-M3C[46] and E0771[47], transduced with H2B-dendra2, a nuclear-localized fluorescent protein. MCa-M3C-H2B-dendra2 (MCa-M3C) or E0771-H2B-dendra2 (E0771) cells are co-injected orthotopically with cellular-scale or tissue-scale PA beads into the mammary fat pad of mice for primary mammary tumors. MCa-M3C cells were co-injected with cellular-scale PA beads tail-vein for metastatic lung tumors (Fig. 1c). Custom-designed, 3D-printed intravital mammary windows (Figure S1) were used in intravital imaging to allow visualization of PA beads and cancer cells via different modes of optical microscopy. For *in vitro* experiments, MCa-M3C cancer cells and PA beads were mixed to form spheroid models (Fig. 1c). Based on the length-scale of the bead and imaging depth requirements, imaging modalities with appropriate spatial resolutions and depth penetrations were used to image the beads embedded within tumors (Fig. 1d): Confocal microscopy was used to image the cellular-scale beads (28.7 ± 18.2 μm) in *in vitro* spheroids and *ex vivo* functional lung models, two-photon microscopy (2P) was used to image *in vivo* cellular-scale beads (28.7 ± 18.2 μm), and optical coherence tomography (OCT) was used to image *in vivo* tissue-scale beads (397 ± 69 μm) (Fig. 1d). To examine whether the presence of the PA beads affects the tumor microenvironment, we performed hematoxylin and eosin (H&E) staining of tumor slices and

observed no distinct fibrosis or inflammation around the PA bead compared to regions far from the bead (Fig. 1e).

To accurately quantify solid stresses in a wide dynamic range, it was critical to tune the Young's modulus of PA beads to a level that would deform in response to the intratumoral solid stress. We used atomic force microscopy (AFM) to measure the Young's modulus of the beads (Fig. 1g), and optimized the Young's moduli of PA beads through multiple *in vitro* and *in vivo* trials using MCa-M3C cancer cells. If the PA beads were too stiff (above 0.77 kPa) (Fig. 1f (i-iii), Figure S19), the resulting deformation was small and unreliable for quantifying a dynamic range of solid stresses in the tumor, and if the beads were too soft (below 0.2 kPa), they do not consistently polymerize and may break or plastically deform in response to solid stress in tumors. We found that PA beads with Young's moduli of E=0.21 ± 0.04 kPa (cellular scale) and E=0.38± 0.15 kPa (tissue scale) resulted in large enough deformations to be detected at the cellular scale and tissue scale, respectively, and can thus detect solid stress levels more sensitively than PA beads with higher Young's moduli (Fig. 1f (iv-vi)). Furthermore, the optimized stiffness values of the PA beads were in the same order of magnitude as cells, spheroids, and tumors and therefore can be appropriately used to estimate the stress experienced by cells (Fig. 1h). Previous studies using PA beads to measure stress have used PA bead Young's modulus values of 0.15-2kPa[31,33,44,45,48], and our bead Young's modulus is on the same order of magnitude as these studies.

We analyzed the deformation in PA beads by determining the absolute value of the principal solid stress tensor in Pascals and elastic energy density in J/m^3 using a 3-D finite element model (FEM) developed in the commercial software ABAQUS (Fig. 1i(iv)). The solid stress distribution and elastic energy density were estimated by quantifying the 3-D deformation field of the originally spherical bead to the geometry obtained through intravital imaging of the PA beads and using the deformation field as the input in FEM (Fig. 1i(ii,iii)) (refer to Methods). We accounted for nonlinear behavior of polyacrylamide[49] under large deformations by directly measuring the nonlinear properties of the hydrogel (Figure S6**Figure S*6*| Nonlinear behavior of polyacrylamide hydrogels. a,** Axial compression curve of polyacrylamide hydrogel. **b,** fitting nonlinear curve to cellular-scale bead Young's modulus of 215 Pa. **c,** fitting nonlinear curve to tissue scale bead Young's modulus of 383 Pa.). For large deformations, using nonlinear elastic properties is essential as we showed that using a hyperelastic nonlinear model results in solid stress values that are 2x higher compared to using a linear model (Figure S7). Analysis of solid stress in FEM requires a priori information about the material properties of PA beads important for stress quantification, notably the Young's modulus and Poisson's ratio[50], which were assumed to be constant throughout the PA beads given the small variation in their material properties (Figure S5). Furthermore, we experimentally determined the Poisson's ratio of polyacrylamide to be 0.22 ± 0.03 by measuring the axial and lateral strain resulting from compressing a bulk polyacrylamide hydrogel. Our parametric study indicated that the Poisson's ratio of 0.22 results in stress response close to a compressible material and that changing the Poisson's ratio between 0 and 0.3 results in less than 60% difference in solid stress (Figure S8). The original diameters of the PA were determined via enzymatic dissociation of tumor tissue to relax bead deformation. For the beads which were embedded in tissues that were not enzymatically dissociated and, therefore, had undeformed diameters that could not be measured exactly, the diameter of the original spherical bead was assumed to be the largest axis length of the deformed bead as a reasonable approximation based on comparisons between the deformed and undeformed diameters of PA beads (Figure S10).

Additionally, to make our solid stress measurement method accessible to users without knowledge of or access to finite element modeling, we also report the aspect ratio of the beads from their 3-D geometry obtained via intravital imaging (Fig. 1i(i)). Given a known and consistent Young's modulus of the beads, we inferred a higher anisotropic solid stress in the deformed beads with higher aspect ratio, which we demonstrate in Fig. 4f. While the aspect ratio of the beads cannot reflect isotropic stresses, this method provided a simple and relative estimate of the anisotropic stress magnitude and direction. To obtain the aspect ratios of the beads, each bead was approximated to an ellipsoid and the three axis length values were obtained (Fig. 1i(i)). The aspect ratio of the PA bead was taken as the ratio of the largest axis length to the smallest axis length.

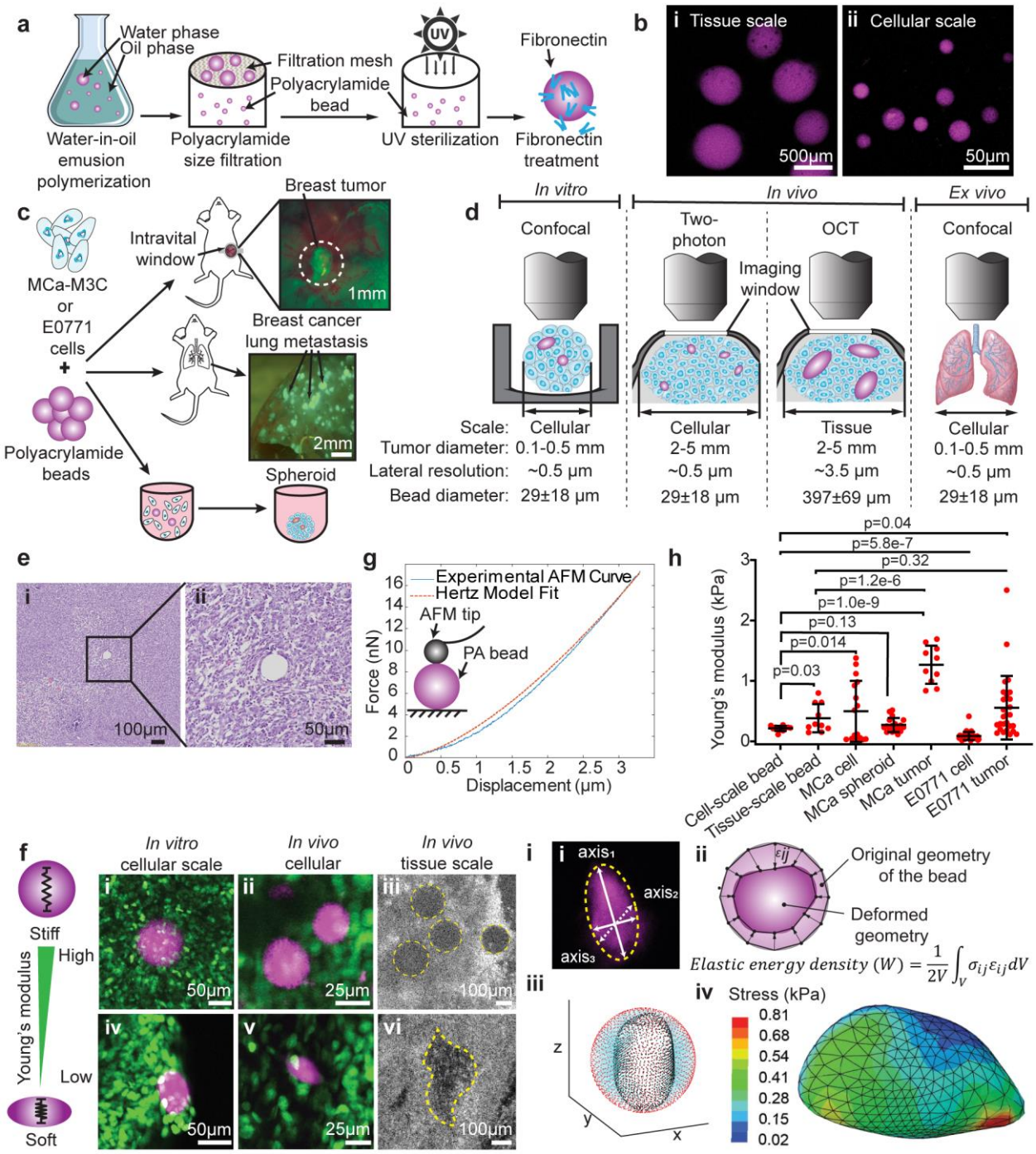

Figure 1|The workflow of *in vivo* solid stress measurement in primary and metastatic tumors. a, PA bead fabrication, filtration, UV sterilization, and treatment with fibronectin. **b,** Rhodamine-labelled PA beads are fabricated at the cellular and tissue scales with diameters of 28.7 ± 18.2 μm (mean ± STD) and 397 ± 69 μm (mean ± STD), respectively. **c,** To probe solid stresses *in vivo*, MCa-M3C or E0771 cells are injected with PA beads into the mammary fat pad of female FVB/NJ mice and an intravital window is implanted to visualize the PA beads and cells. To probe solid stresses in lung metastases, MCa-M3C cells are injected with PA beads into the tail-vein of female FVB/NJ mice. To probe solid stresses *in vitro*, MCa-M3C cells are seeded with PA beads to form spheroids in low-attachment round-bottom wells. Fluorescent tumors were visualized using a fluorescent stereomicroscope. **d,** Multi-modal intravital microscopy including confocal, two-photon, and optical coherence tomography, was used to probe solid stresses *in vitro*, *in vivo* at the cellular scale, and *in vivo* at the tissue scale, respectively. Additionally, *ex vivo* functional lungs were imaged using confocal. **e,** H&E staining shows the region around the embedded PA beads is similar to regions far from the void, demonstrating no additional fibrosis or inflammation due to PA beads. **f,** The PA bead Young's modulus was optimized at each scale to achieve sensitive measurements of solid stress **(i,ii,iv,v)** cancer cells (green), PA beads (magenta), **(iii,vi)** PA bead (dark gray, yellow dotted outline)). Beads with high Young's modulus, E=1.27 ± 0.3 kPa in **(i)**, E=1.27 ± 0.3 kPa in **(ii)**, and E=3.44± 0.3kPa in **(iii)** do not deform in response to solid stresses, and hence will not be sensitive to stresses. The optimal Young's moduli that sensitively deform in response to solid stresses are determined as E=0.21 ± 0.04 kPa for cellular scale *in vitro* **(iv)**, E=0.21 ± 0.04 kPa for cellular scale *in vivo* **(v)**, and E=0.38± 0.15 kPa for tissue scale *in vivo* **(vi)**. **g,** PA bead Young's moduli were measured using AFM and fitting of a Hertz model. **h,** AFM measurements of Young's modulus of cellular- and tissue-scale PA beads (mean ± STD, n=10-11 beads, two-tailed Student's t-test), in comparison with Young's modulus of individual cells, spheroids, and mammary tumors (mean ± STD, n=16 MCa-M3C single cells, n=18 MCa-M3C spheroids (50k cells/spheroid), n=10 tumor regions across N=3 MCa-M3C tumors, n=37 E0771 cells, n= 27 regions across N=2 E0771 tumors, two-tailed Student's t-test). **i,**

Quantification of solid stress by **(i)** fitting an ellipsoid to obtain 3 axis diameters representing the PA bead and measuring the aspect ratio of PA beads as a simple and accessible readout. The **(ii)** elastic energy density (W) and **(iv)** solid stress spatial distributions are quantified through mathematical modeling by determining the **(iii)** deformation of the bead from the undeformed spherical geometry and finite element analysis.

Validation and sensitivity analysis of the solid stress measurement method *in vivo*

Using intravital microscopy of deformable PA beads, we quantified the PA bead aspect ratios and the principal solid stresses in *in vivo* murine tumors at the cellular and tissue scales in 3-D. Tumors with cellular-scale beads were formed separately from tumors with tissue-scale beads, and the same batch of cellular and tissue scale beads were used across all experiments for consistency. We measured the bead aspect ratios after pushing them through 25G and 23G needles (for cellular and tissue scale, respectively) used for tumor injections and our analysis indicates that the beads exhibited an aspect ratio of approximately 1 before injecting them into mice (Figure S3). When PA beads are injected into the mammary fat pad without cancer cells and immediately imaged, the aspect ratios of the beads are 1.26 ± 0.10 (Figure S3), suggesting that there is a baseline level of mechanical stress applied to the spheres by surrounding normal tissues. 5-7 days after injecting the PA beads and MCa-M3C or E0771 cancer cells into the mammary fat pad of mice, we observed unexpectedly dramatic deformations in the PA beads *in vivo* using OCT (tissue-scale) (Fig. 2a, d) and 2-photon microscopy (cellular-scale) (Fig. g, j). Prior to enzymatic treatment, in MCa-M3C tumors, PA beads had stresses of 2.24 ± 0.736 kPa and aspect ratios of 3.41 ± 0.59 (mean ± STD, N=4) at the tissue scale (Fig. 2b, c), and stresses of 0.195± 0.128 kPa and aspect ratios of 1.87 ± 0.42 (mean ± STD, N=3) at the cellular scale (Fig. 2h, i). In E0771-H2B-dendra tumors, we observed stresses of 0.755 ± 0.289 and aspect ratios of 3.2± 0.480 (mean ± STD, N=3) at the tissue scale (Fig. 2e, f) and stresses of 0.161 ± 0.059 kPa and aspect ratios of 2.07 ± 0.389 (mean ± STD, N=4) at the cellular scale (Fig. 2k,l). Thus, we next sought to determine if the deformation was plastic (irreversible) or elastic (reversible), and if the beads were still intact or broken. To investigate this, we used enzymatic dissociation of the tumor as an effective method to relax the intratumoral solid stresses[11,24,29,51,52] to observe the relaxation of the highly deformed PA beads to their original stress-free geometry. For the *in vivo* setting, we used a solution of collagenase and hyaluronidase immediately post-euthanasia *in situ*, and longitudinally imaged the relaxation of the solid stress reflected by a change in the geometry of the PA beads using two-photon microscopy and OCT. For the *in vitro* setting, we used trypsin instead of collagenase and hyaluronidase to dissociate the spheroids since trypsin was sufficient for complete spheroid dissociation. At both the tissue and cellular scales *in vivo* and at the cellular scale *in vitro*, we observed significant decreases in stresses before and after enzymatic treatment (Fig. 2 b,e,h,k) and that the beads converge towards the original spherical geometry represented by the aspect ratio of 1 (Fig. 2c,f, i, l). After enzymatic treatment, in MCa-M3C tumors, PA beads had stresses of 0.282 ± 0.165 kPa and aspect ratios of 1.81 ± 0.493 (mean ± STD, N=4) at the tissue scale, and stresses of 0.130 ± 0.088 kPa and aspect ratios of 1.56 ± 0.336 (mean ± STD, N=3) at the cellular scale. In E0771-H2B-dendra tumors, we observed stresses of 0.135 ± 0.071 kPa and aspect ratios of 1.51 ± 0.248 (mean ± STD, N=3) at the tissue scale and stresses of 0.097 ± 0.051 kPa and aspect ratios of 1.67 ± 0.323 (mean ± STD, N=4) at the cellular scale. This result showed that the PA beads, even being highly deformed to aspect ratios of around 4, undergo primarily reversible and elastic deformation. In 2-3 hours, the stresses that accumulated in the tissues for 5-7 days could be relaxed using enzymatic dissociation of tissue. While the beads relaxed to an aspect ratio of close to 1 in the *in vitro* spheroids where enzymatic dissociation was more effective, the *in vivo* beads did not fully relax to an exact aspect ratio of 1 potentially due to residual stresses that may have remained due to incomplete dissociation of surrounding tissue (Figure S3). We did not fully dissociate the tissue mechanically after enzymatic dissociation in order to maintain the relative position of beads during longitudinal tracking of the beads over the course of enzyme dissociation. In the time and length scales of this study, the viscoelastic effects are negligible since the relaxation time of polyacrylamide is much shorter (< 2 minutes; Figure S9) than the 2-3 hours of stress relaxation by enzymatic dissociation. Thus, the PA beads underwent a dramatic but reversible deformation demonstrating that this method can be used to sensitively measure a wide range of solid stress magnitudes in tumors, from ~0.1-4kPa.

We next investigated if euthanasia affected the measurement of solid stress. We euthanized mice to relax the elevated tumor interstitial fluid pressure[36,53], which originates from blood pressure and converges to zero post-mortem[54,55] and compared the deformation of the PA beads *in vivo* versus 60 minutes post-mortem.

At both the cellular and tissue-scales, solid stress measured up to 60 minutes after euthanasia closely reflected the *in vivo* solid stress values (Fig. 2o).

Finally, we optimized and validated our tumor induction approach to exclude any potential artifact, e.g., artificial compression exerted by the window. We compared the solid stress at the cellular level in tumors that were induced after the implantation of the imaging window versus tumors growth without any imaging window to avoid potential artificial compression. We did not observe any significant difference between the solid stress in these two tumor induction methods (Fig. 2p) and concluded that tumor induction under the imaging window did not alter the intratumoral solid stresses. We observed that if the imaging window was implanted over established tumors, the window may artificially compress the tumor and generate an artifact in the solid stress field (Figure S4). Hence, for studies relevant to the physical tumor microenvironment, implantation of windows over established and large tumors should be avoided.

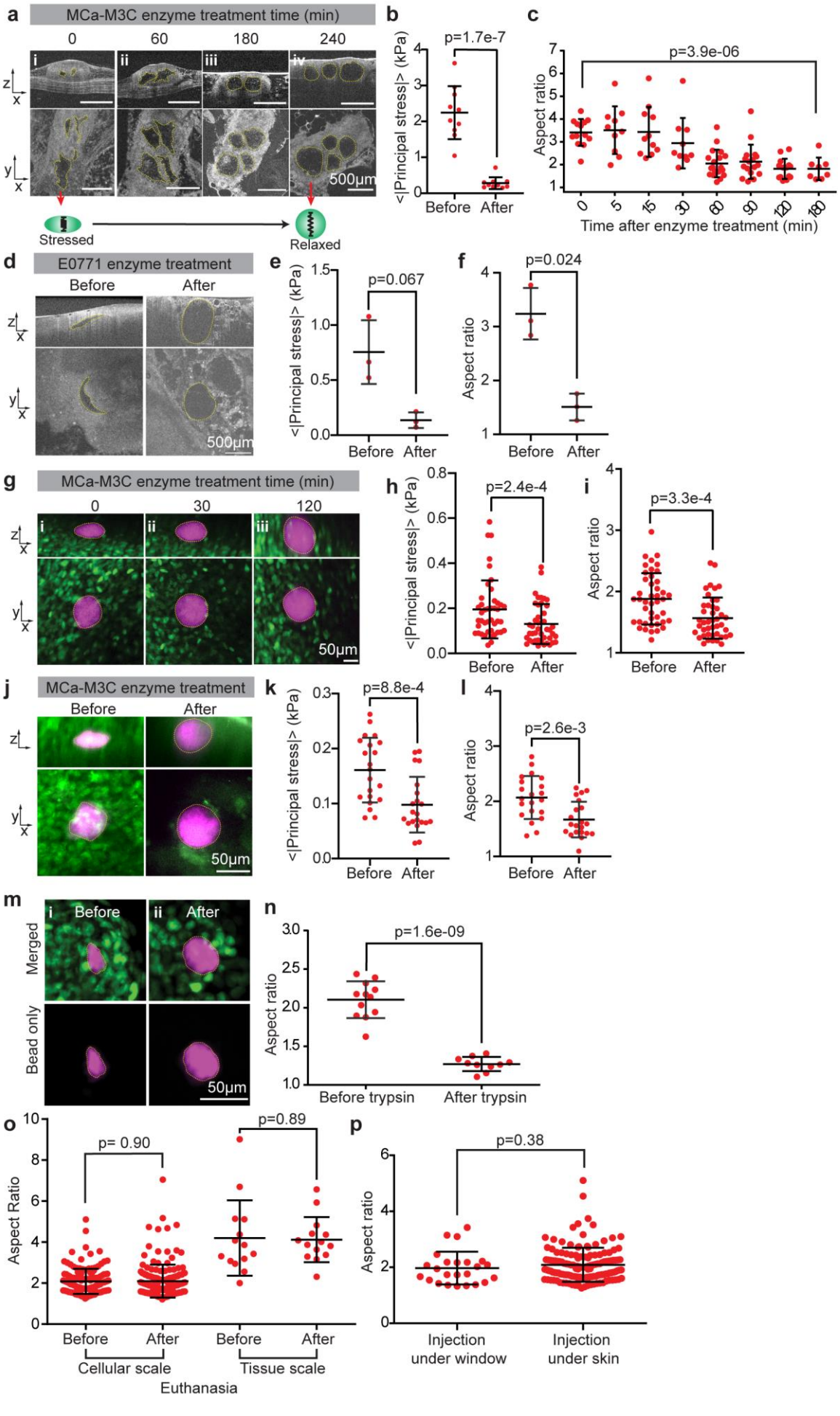
a
MCa-M3C enzyme treatment time (min)
0
60
180
240
i
ii
iii
iv
z
x
y
x
500μm
Stressed
Relaxed
b
p=1.7e-7
<|Principal stress|> (kPa)
Before
After
c
p=3.9e-06
Aspect ratio
Time after enzyme treatment (min)
d
E0771 enzyme treatment
Before
After
500μm
e
p=0.067
<|Principal stress|> (kPa)
f
p=0.024
Aspect ratio
g
MCa-M3C enzyme treatment time (min)
0
30
120
50μm
h
p=2.4e-4
<|Principal stress|> (kPa)
i
p=3.3e-4
Aspect ratio
j
MCa-M3C enzyme treatment
Before
After
50μm
k
p=8.8e-4
<|Principal stress|> (kPa)
l
p=2.6e-3
Aspect ratio
m
i Before
ii After
Merged
Bead only
50μm
n
p=1.6e-09
Aspect ratio
Before trypsin
After trypsin
o
p= 0.90
p=0.89
Aspect Ratio
Before
After
Before
After
Cellular scale
Tissue scale
Euthanasia
p
p=0.38
Aspect ratio
Injection under window
Injection under skin

Figure 2| Validation and sensitivity analysis of solid stress measurement at the cellular and tissue scales *in vivo.* a, Relaxation of solid stresses at the tissue scale was demonstrated by enzymatic treatment (collagenase/hyaluronidase) of the MCa-M3C tumor *in situ* post-euthanasia and imaging of the beads with optical coherence tomography (OCT) (PA beads marked with yellow dotted line). Tracking of highly deformed beads relaxing to near-spherical geometry demonstrates the presence of extremely high stresses that were able to deform the PA beads. The reversibility of PA bead deformation (**i** to **iv**) demonstrates their sensitivity and wide dynamic range of solid stresses that can be quantified from their experienced deformation. **b,** Stress and **c,** aspect ratio decreases after 180 minutes of enzymatic treatment (mean ± STD, N=2-4 mice, n=8-19 beads, two-tailed Student's t-test). **d,** Representative image of the reversibility of bead deformation after enzymatic treatment in E0771 tumors. **e,** Stress and **f,** aspect ratio changes after 240 minutes of enzymatic treatment (mean ± STD, N=3 mice, n=3 beads, two-tailed Student's t-test). **g,** Representative two-photon images from administration of collagenase/hyaluronidase enzyme at the cellular scale *in situ* (cancer cells (green), PA beads (magenta)). **h,** Stress decreases and **i,** aspect ratio of the cell-scale beads converges toward 1 (spherical geometry) after 120 minutes of collagenase/hyaluronidase treatment (mean ± STD, N=3 mice, n=4 beads, two-tailed Student's t-test). **j,** Representative two-photon images before and after enzymatic treatment of cellular-scale beads in E0771 tumors. **k**, Stress and **l,** aspect ratio of PA beads decrease after 240 minutes of enzymatic treatment (mean ± STD, N=4 mice, n=21 beads, two-tailed Student's t-test). **m,** Representative confocal images of a spheroid embedded with a polyacrylamide bead before and after trypsin treatment (cancer cells (green), PA beads (magenta)). **n,** Stress relaxation after 240 minutes of trypsin treatment. (mean ± STD, n=13-36 beads, two-tailed Student's t-test). **o,** Euthanasia and the consequent changes in IFP does not significantly change the solid stress levels at the cellular and tissue scale 60 minutes after euthanasia (mean ± STD, N=4 mice, n=14-21 beads, two-tailed Student's t-test). **p,** After injecting tumor cells under an already implanted window, we found that the presence of the imaging window chamber does not alter the solid stresses measured at the cellular scale (mean ± STD, N=4-7 mice, n=33-151 beads, two-tailed Student's t-test).

Scale-dependent transmission of solid stresses in primary breast tumors

Tumors have heterogeneous mechanical properties and architecture across different length scales[56,57]. We used our *in vivo* solid stress measurement method to investigate if solid stresses are length-scale dependent in two models of murine breast tumors. To measure solid stresses at the cellular and tissue scales, the PA bead sizes were fabricated to mimic cellular- and tissue-length scales (28.7 ± 18.2 μm and 397 ± 69 μm in diameter, respectively (Fig. 3a)). The elastic energy density and the principal stresses at the tissue scale was measured to be higher (5.2x and 8.5x in MCa-M3C, respectively 4.3x and 5.3x in E0771, respectively) than that of the cellular scale (Fig. 3b,c). The difference in stress at the two scales was unexpected, as the stress (force normalized by area), and strain energy density (elastic energy normalized by volume) do not depend on the scale of measurement in homogeneous and linear materials. Furthermore, when compared to solid stress values quantified via previous *ex vivo* methods[28,29], the *ex vivo* quantification of solid stress is within the range of cellular-scale stresses, but vastly underestimates tissue-scale stresses (Fig. 3c), demonstrating that in the previous *ex vivo* methods, the components of solid stress were only partially measured. Using a simplified quantification of solid stress via the measurement of aspect ratios, we also observed that tissue scale PA beads were deformed at higher aspect ratio than the cell scale beads (2x in MCa-M3C and 1.7x in E0771) (Fig. 3d). The factor of difference in aspect ratios measured at the cellular vs tissue scale (2x and 1.7x) is lower than the factor of difference in the principal stresses (8.5x in MCa-M3C and 5.3x in E0771). The difference in Young's moduli between the cellular-scale and tissue-scale beads likely contributes to this discrepancy since the tissue-scale PA beads have a higher Young's modulus compared to cellular-scale PA beads (Young's modulus of 0.215 ± 0.042 kPa at the cellular scale and 0.383 ± 0.234 kPa at the tissue scale), yet is not responsible for the observed scale-dependence. The difference in the Young's moduli is accounted for in the stress quantification of the PA beads and therefore it is more accurate to measure solid stress via stress quantification where the Young's modulus is accounted for rather than measuring aspect ratio alone. With that in consideration, we expect that using cellular- and tissue-scale beads with the same Young's moduli would allow aspect ratio to be a more comparable reflection of the differences quantified using absolute solid stress. Nonetheless, aspect ratio is a useful quantity to measure since it provides information on stress anisotropy, as we will explain in further sections. Additionally, in both tumor models, we observe that cellular-scale beads of 28.7 ± 18.2 μm in the same tumor have an increasing trend in aspect ratio as the PA bead diameter increased (Fig. 3e), further demonstrating the scale-dependence of solid stress in tumors. In the bulk of our analysis, the elastic energy density and solid stress values were obtained by approximating the PA beads to ellipsoids, but by using the original deformed geometry of the bead in our FEM model, we demonstrate that at the cellular-scale, beads experienced a narrow range of stresses (0.004-0.574 kPa), whereas tissue-scale beads experienced a wider range and larger magnitude of stresses (0.282-2.55 kPa) (Fig. 3f). By using the original deformed geometry of the bead, we were able to capture differences in spatial heterogeneity experienced at the cellular and tissue scales; we showed that the tissue-scale measurements capture heterogeneity in solid stresses, whereas the solid stresses experienced at the cellular scale are comparatively more uniform.

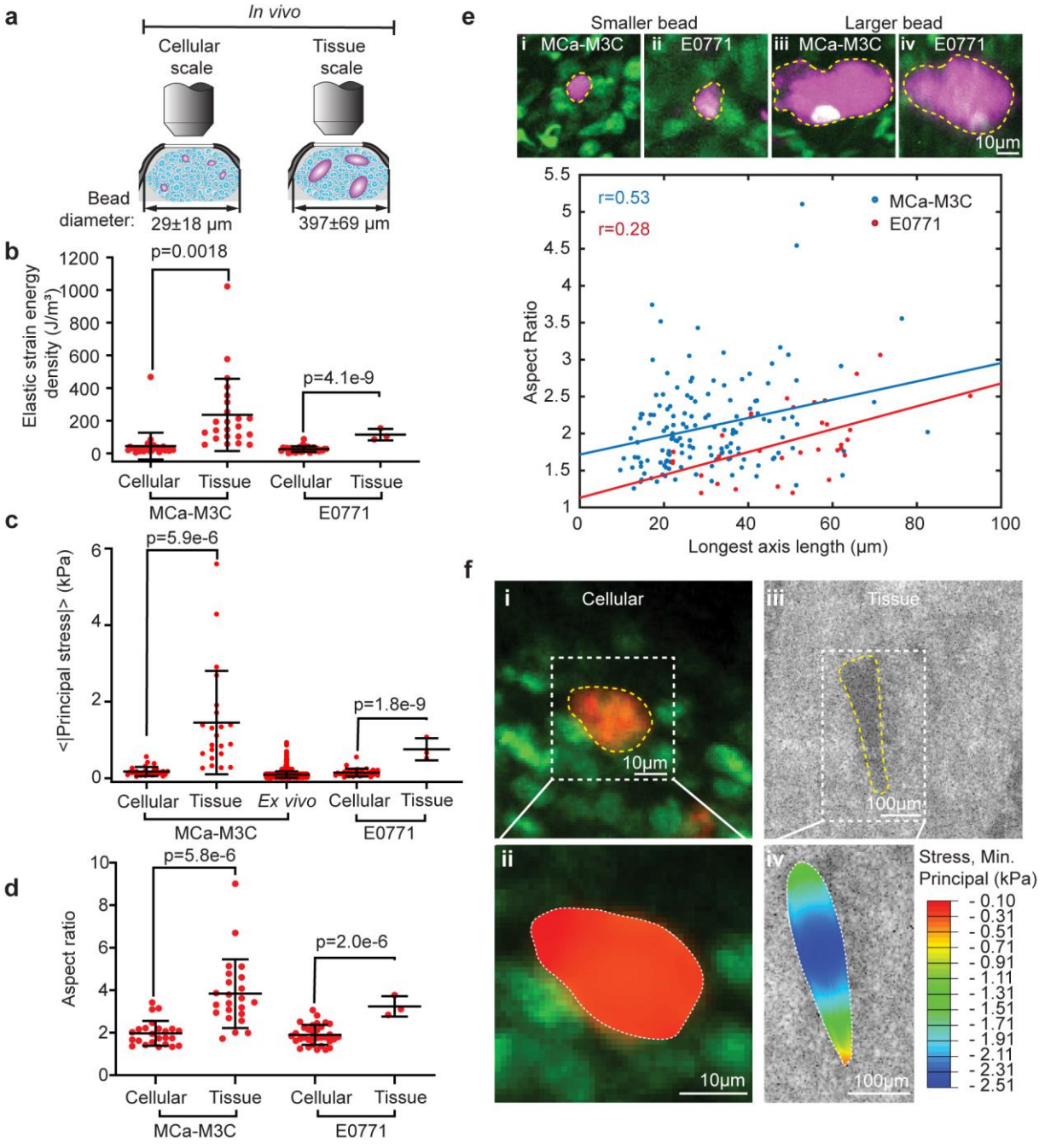

Figure 3| Solid stress transmission is scale-dependent: *In vivo* solid stresses experienced by cancer cells at the cellular scale is significantly lower than solid stresses experienced at the tissue scale. a, Measuring solid stresses across an order of magnitude different scales. **b,** Elastic energy density of *in vivo* tumors at the tissue scale (236 ± 220 J/m^3 (MCa-M3C) and 115 ± 35 J/m^3 (E0771)) is higher than the cellular-scale energy density (45.1 ± 81.9 J/m^3 (MCa-M3C) and 27 ± 17 J/m^3 (E0771)) by approximately a factor of 5.2 in MCa-M3C (mean ± STD, N=5 mice, n=23-29 beads, two-tailed Student's t-test) and 4.3 in E0771 (mean ± STD, N=3-4 mice, n=3-33 beads, two-tailed Student's t-test). **c,** Principal stresses of *in vivo* tumors is 8.5x higher at the tissue scale (1.45 ± 1.35 kPa) compared to the cellular scale (0.172 ± 0.12 kPa) in MCa-M3C (boxplot, N=5 mice, n=23-29 beads, two-tailed Student's t-test) and is 5.3x higher at the tissue scale (0.755 ± 0.288 kPa) compared to the cellular scale (0.148 ± 0.102 kPa) in E0771 (boxplot, N=3-4 mice, n=3-33 beads, two-tailed Student's t-test). Comparison with the solid stress range (σ_{zz} =0.09 ± 0.08 kPa) in an *ex vivo* tumor from previous methods[28,29] demonstrates that *ex vivo* methods do not represent the full range of 3-D solid stresses in an *in vivo* tumor. **d,** Aspect ratios of the polyacrylamide bead *in vivo* at the tissue scale is 2x higher compared to the cellular scale in MCa-M3C (mean ± STD, N=5 mice, n=23-29 beads, two-tailed Student's t-test) and 1.7x higher in E0771 (mean ± STD, N=3-4 mice, n=3-33 beads, two-tailed Student's t-test). **e,** Scale-dependence of polyacrylamide bead deformation within cellular-scale sized beads imaged in the same tumor by two-photon microscopy (cancer cells (green), PA beads (magenta). Positive relationship of aspect ratio with increasing polyacrylamide bead diameter in MCa-M3C (n=143 beads, linear regression line, Pearson correlation, r=0.28, p-value=6.5x10^{-4}) and in E0771 (n=33 beads, linear regression line, Pearson correlation, r=0.53, p-value=0.0015). When cellular-scale polyacrylamide beads, which varied from 28.7 ± 18.2 μm in diameter, were used, the increasing trend in scale-dependence with solid stress is consistent with the results reported in (**b-d**). **f,** Finite element modeling of polyacrylamide beads enables quantification of the spatial distribution of solid stresses at the cellular and tissue scales (**(i)** cancer cells (green), PA beads (red), **(ii)** Overlay of cellular-scale FEM stress-distribution cross-section, **(iii)** PA bead (yellow dotted outline)). **(iv)** Overlay of tissue scale FEM stress-distribution cross-section.

Longitudinal and spatial measurements of solid stresses *in vivo* at the cellular scale

The mechanical properties of tumors change with tumor growth and vary spatially. Our measurement system is capable of measuring longitudinal and spatial measurements in tumors *in vivo*. We demonstrate the longitudinal measurement of cellular-scale solid stress in E0771 tumors over 6 days post-injection (Fig. 4a). Solid stress and aspect ratio increase from day 0 to day 2 and plateau from days 2 through 6 (Fig. 4b,c), revealing that solid stress accumulation at the cellular-scale occurs rapidly within the first two days of tumor formation. Our method allows longitudinal monitoring of cellular-scale and tissue-scale stresses up to 7 and 14 days, respectively (Figure S2). Tumor growth and fibrosis occurring in response to window implantation caused beads to be obscured beyond the depth of imaging and limited the timeframe allowed for longitudinal imaging of PA beads, but we show that window implantation does not affect the measurement of solid stress (Fig. 2p). Due to the higher penetration depth of ~2mm for OCT compared to ~200µm for 2-photon microscopy, the number of days in which beads could still be visualized was longer for the tissue scale (Figure S2). In addition to longitudinal measurements, the system can measure solid stress spatially in X,Y, and Z positions. We show that solid stress does not vary as a function of depth (in the Z-direction) over 160 µm (Fig. 4d,e). This may be due to the limitation of microscopy, which limits imaging to only a few hundred microns deep in the Z-direction, which is not deep enough to observe variations in solid stress as the beads which are being imaged are in the periphery of the tumor. We further show that our approach enables mapping of the heterogeneities of solid stress in the XY direction in the tumor (Fig. 4g,h). Additionally, we find that stress has a linear relationship with aspect ratio, showing that for beads experiencing anisotropic stress, aspect ratio provides information on the relative stresses in the tumor (Fig. 4f).

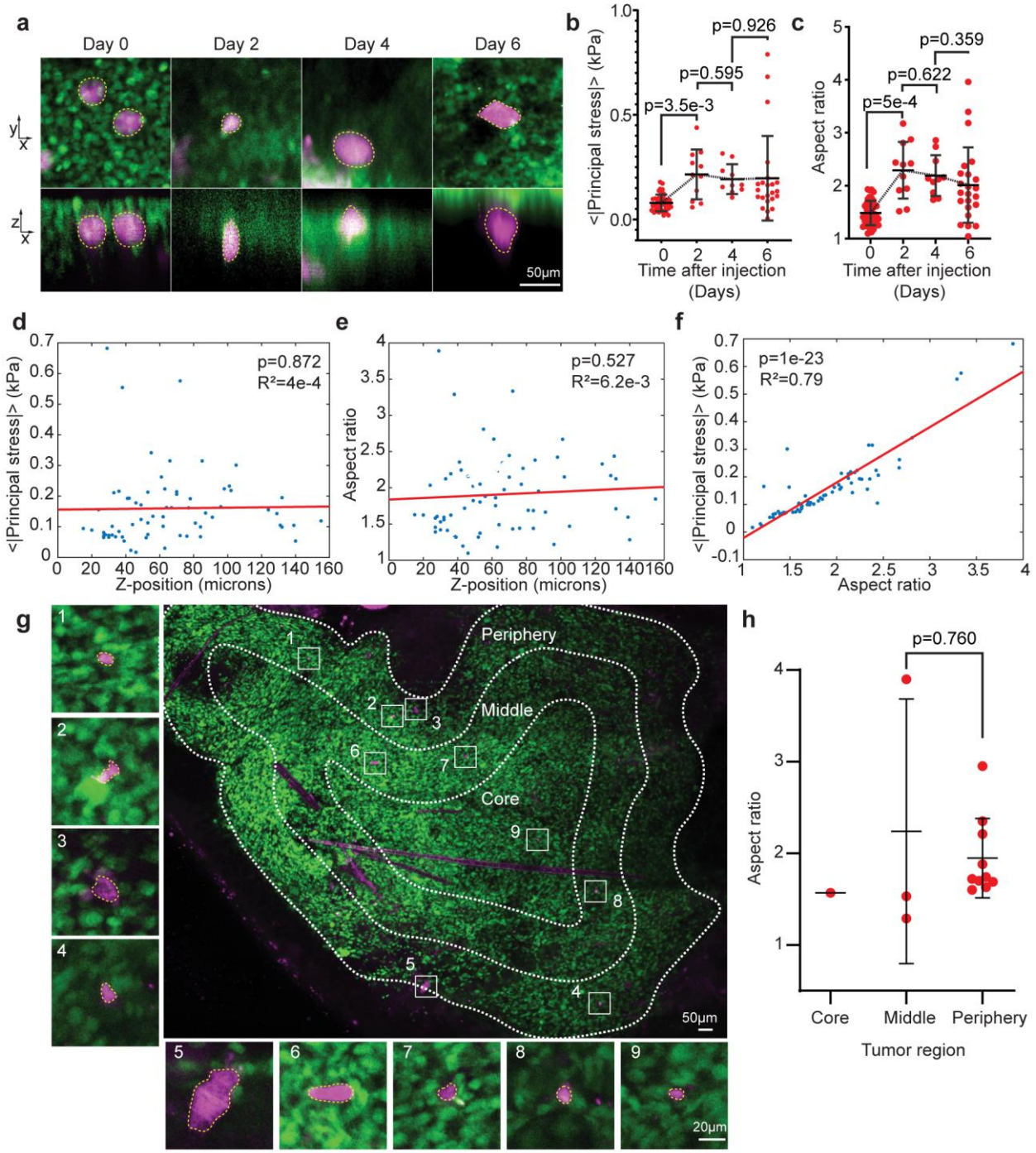

Figure 4| Longitudinal and spatial measurements of solid stresses *in vivo* at the cellular scale. a, Representative images of cellular-scale beads in E0771 tumors at 0, 2, 4 and 6 days after tumor induction. **b,** Longitudinal stress and **c,** aspect ratio of PA beads over 6 days after injection of PA beads and cancer cells on day 0 (mean ± STD, N=3 mice, n=10-42 beads). **d,** Stress and **e,** aspect ratio as a function of the z-position of the bead relative to the surface of the tumor, where is z=0 (n= 67 beads, linear regression). **f,** Stress and aspect ratio have a positive linear relationship (n=67 beads, linear regression). **g,** Mapping PA beads across an E0771 tumor at the core, middle and periphery of the tumor. **h,** Aspect ratios of PA beads in regions defined by equidistant offset from the tumor boundary (mean ± STD, N=1 mouse, n=1-10 beads).

Cellular-scale measurements of solid stresses in lung metastases

In both human and murine breast cancer lung metastasis, a hallmark of the physical microenvironment is solid stress accumulation resulting in vessel compression[12,14]. Given that there is evidence that metastatic and primary tumors, despite originating from the same cancer cells, have distinct reponse to treatment[58], we

quantified solid stress in the breast cancer lung metastasis. While the physical microenvironment of metastatic tumors have been characterized in liver[29] and brain[21] tissues, the mechanical environment of lung metastasis is more challenging to study due to the complex structure of the lung and the small scale of micrometastases. To measure solid stress in metastatic lung tumors, we co-injected cellular-scale PA beads with the same breast cancer cells as the primary tumor experiments (MCa-M3C) into the tail-vein of FVB mice. The goal was to have the fluorescent PA beads and cancer cells travel through circulation to the lung and form a metastatic tumor. By measuring the deformation of the bead, we then estimated the solid stresses present in the breast cancer lung metastasic tumors. After approximately 1-2 weeks, we sacrificed the mice and extracted the whole lung for *ex vivo* imaging of the pleural lung surface. Interestingly, the beads were stochastically sequestered in the lung vasculature in regions with and without metastatic cancer nodules. The beads, with average diameters of 29μm, are arrested at the arteriole-capillary junction as they are too large to travel through pulmonary capillaries (Fig. 5a). Since the beads are at the same scale and have a similar Young's modulus as cancer cells[59] (Fig. 1h), the bead deformation reflects the stresses that single cancer cells experience inside small vessels in the lung. The stresses are cyclic in a respiring lung, causing the cells traveling through lung vasculature to experience different magnitudes of cyclical mechanical stresses *in vivo*, which may activate biological pathways[60-62]. We measured the aspect ratios and stresses of PA beads in the lung tumors at alveolar pressures of 3 and 18 cmH_2O and compared the measured stresses with the stress in primary tumors from the same cell line (MCa-M3C) and observed that the cellular-scale stress and bead aspect ratios within lung metastases at 18cmH_2O are significantly higher than stresses in primary tumors (Fig. 5b). These results indicate that the tissue environment of the cancer cells significantly affects the stresses that are experienced by the cancer cells. Furthermore, we investigated if the stresses in the lung metastases vary by spatial location. We compared the bead aspect ratios in the intratumor, peritumor and non-tumor regions and show that the peritumor has significantly higher aspect ratios compared to non-tumor and intratumor regions (Fig. 5d). However, no significant difference exists between bead aspect ratios in the intratumor and non-tumor intravascular regions. Our observation that the core of tumors experience isotropic stresses, whereas tensional stresses at the periphery cause anisotropy is in consensus with what has been reported in literature[35,63].

The measurement of solid stress in the lung is limited to the cellular-scale. To investigate whether beads of larger diameters could be used to measure tissue-scale stresses, we injected 140-280μm diameter PA beads via tail vein (

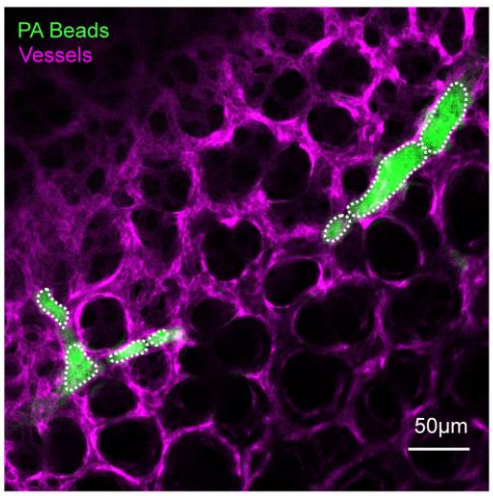

Figure ***S15***). Within 5 minutes, we noticed shallow respiration of the mouse, denoting the lethality of large PA bead injection into the vasculature. The mouse was euthanized and upon imaging the lung, we noticed blockage of arterioles in the lung by large beads via imaging. Therefore, macroscale measurements are not possible within the lung vasculature, as PA beads of 140-280μm do not freely flow through the small vessels in the lung.

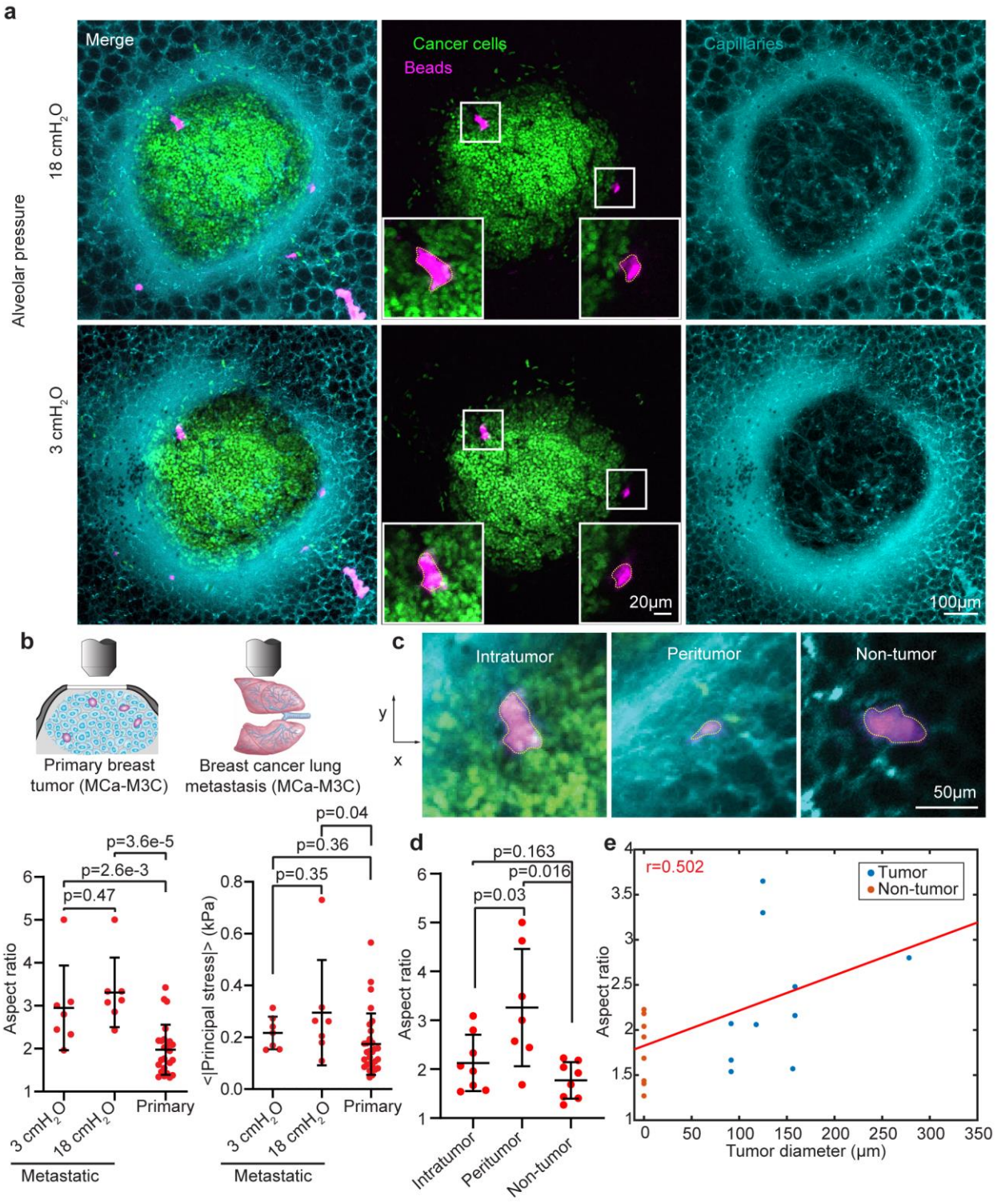

Figure 5| Measurement of solid stress in breast cancer lung metastases in a functioning lung. a, Representative images of cellular-scale beads in a metastatic nodule in the lung at two different alveolar pressure relevant to the breathing cycle. **b,** The aspect ratios and solid stress of the PA beads in lung metastases at alveolar pressures of 3 and 18 cmH_2O (mean ± STD, N=3 mice, n=7 beads) compared to cellular-scale bead aspect ratios in primary tumor; solid stresses in metastatic tumors are higher than primary tumors despite being induced by the same MCa-M3C cancer cells (mean ± STD, N=2-5 mice, n=29 beads, two-tailed Student's t-test). **c,** Representative images of PA beads in the intratumor, peritumor and intravascular regions of the lung. **d,** Aspect ratios of PA beads in the intratumor, peritumor and regions far from the tumor at 3 cmH_2O alveolar pressure (mean ± STD, N=4 mice, n=7-8 beads, two-tailed Student's t-test). **e,** Aspect ratios of the PA beads as a function of lung tumor nodule diameter (N=4 mice, n=18 beads, linear regression line, Pearson correlation, r=0.502, p-value=0.033) demonstrating elevated solid stress in tumor diameters as small as 100-300 μm

Measurement of solid stress experienced by single cells in lung vasculature

Cancer cells migrate through the vasculature prior to arriving at the site of metastasis, and are arrested in capillaries during the early stages of lung metastasis. We were interested in quantifying the forces experienced by cancer cells in capillaries. Using PA beads with similar size and material properties as circulating cells, which are measured a priori, allows us to mathematically model the deformations and stresses that cancer and immune cells experience in lung vasculature. We also measured the stresses inside lung vasculature at varying alveoli pressures. We imaged the PA beads at physiological alveolar pressures of 18, 12, 7 and 3 cmH_2O during a breathing cycle of a functional lung[64,65], and quantified the aspect ratios of the PA beads and their corresponding stress values (Fig. 6a). The magnitude of solid stress that the beads experience was estimated via finite element modeling to be as high as 0.73 kPa (Fig. 6b), which resulted in substantial deformation in the PA beads. To our knowledge, this is the first direct estimation of the stresses that a circulating cell, cancer or immune cell, experiences inside the pulmonary microvasculature. The aspect ratio and stress both increase as a function of relative diameter, which is the largest diameter of the bead normalized to the diameter of the vessel (Fig. 6c,d). The vessels experience different changes in diameter as we increased the alveolar pressure from 3 to 18 cmH_2O. The resulting PA bead aspect ratios and stresses depended on the change in vessel diameter (Fig. 6e). Beads in vessels that underwent large vessel diameter changes were less deformed from 3 to 18cmH_2O whereas beads in vessels with smaller diameter changes generally had increased aspect ratios as alveolar pressure increased from 3 to 18cmH_2O. Our method shows that PA beads are sensitive to changes in solid stress even when deformed in vessels, which allows the method to be used to detect cyclical changes in vasculature during respiration to determine the changes in solid stress experienced by cells in vessels. We compared the stresses and aspect ratios of the PA beads at alveolar pressures of 3 and 18cmH_2O and found that there is no significant difference in either stress or aspect ratio (Fig.6f,g). This method used to estimate the stresses applied on the circulating cells in the lung capillaries can be extended to estimate the solid stresses that immune cells experience during their sequestration in the lung capillaries, which may affect their function[64], and can also measure stress in other major sites of metastasis where the PA beads can be delivered, such as the brain and liver (Figure S18).

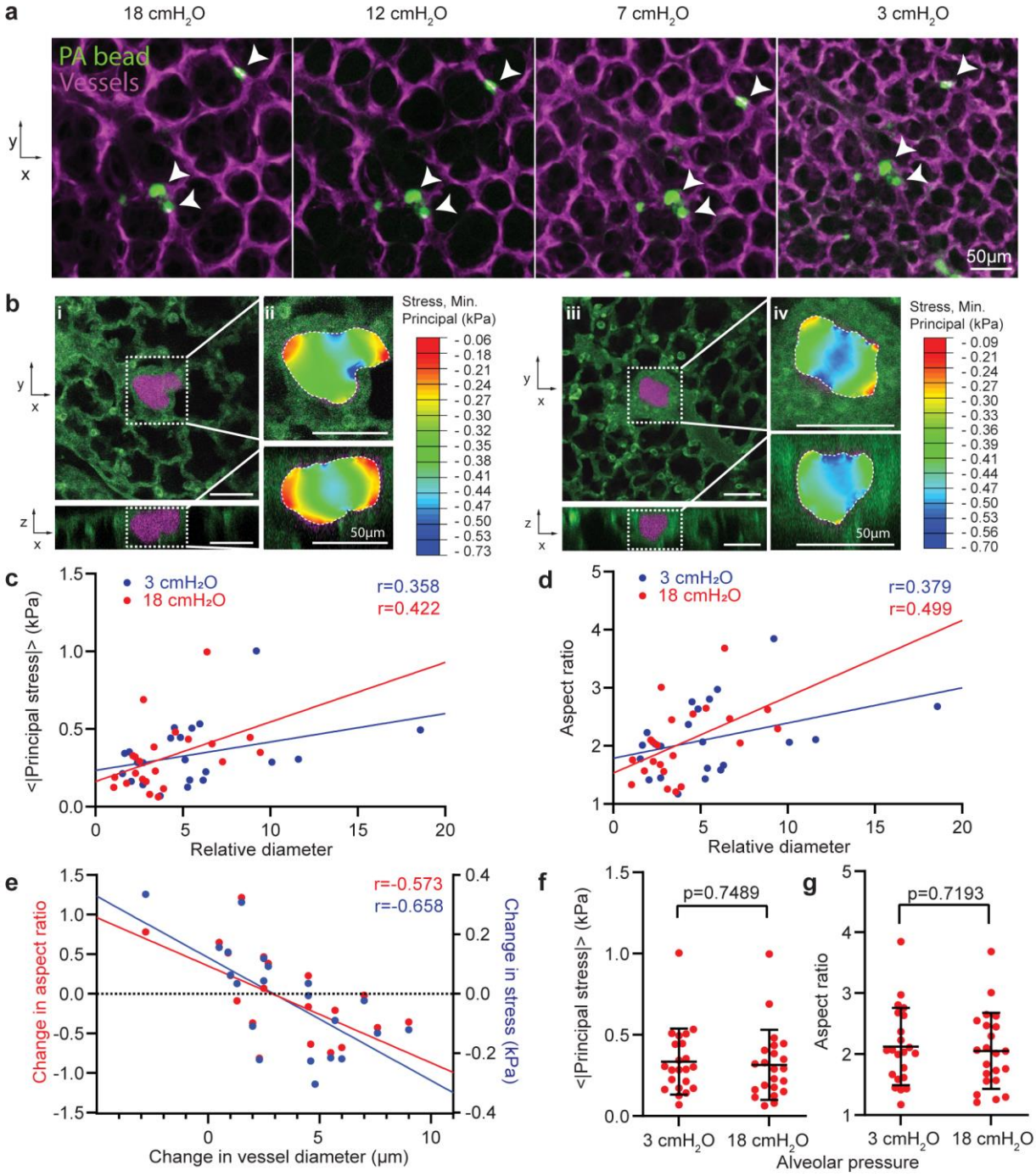

Figure 6| Measurement of solid stresses that individual cells experience in blood vessels using cellular-scale beads as surrogates for single cells. a, Representative images of PA beads arrested in functional lung vasculature at alveolar pressure of 18, 12, 7 and 3 cmH_2O. **b, (i,iii)** The PA beads with similar size and stiffness as the individual cancer cells traveled to the lung through the blood circulation and arrested in microvasculature (lung autofluorescence from extracellular matrix proteins (green), PA beads (magenta)). **(ii, iv)** Knowing the non-deformed geometry and material properties of the PA bead, we used finite element modeling to map solid stresses that PA beads experience at high-resolution, indicating stresses as high as 0.73 kPa that cancer cells experience during their microvascular arrest in lung metastasis (lung autofluorescence (green), PA beads (magenta)). **c,** The stresses and **d,** aspect ratios of the PA beads increase with increasing relative diameter, which is the largest diameter of the PA bead normalized to the diameter of the vessel (N=3 mice, n=22 beads, blue: 3cmH_2O, red: 18cmH_2O, linear regression line, Pearson correlation, c: r=0.358, p-value=0.102 (3cmH_2O), r=0.422, p-value=0.050 (18cmH_2O) , d: r=0.379, p-value=0.0.082 (3cmH_2O), r=0.499, p-value=0.018 (18cmH_2O)). **e,** Change in aspect ratio and stress as a function of the change vessel diameter from 3 to 18cmH_2O. In vessels which have larger positive changes in vessel diameter, the aspect ratio of the PA beads decreases, whereas in vessel that have smaller changes in diameter, the aspect ratios of the PA beads increase with pressure change (N=3 mice, n=22 beads, linear regression line, Pearson correlation, change in aspect ratio: r=-0.573, p-value=0.0053, change in stress: r=-0.658, p-value=8.68×10^{-4}). . **f,** Stress and **g,** aspect ratio of PA beads at 3 and 18 cmH_2O (N=3 mice, n=22 beads, paired two-tailed Wilcoxon matched-pairs signed rank t-test).

In vitro 3-D cancer model recapitulates *in vivo* tumor solid stress at the cellular scale

Spheroid and organoid models of tumors are increasingly popular *in vitro* models of cancer as they better recapitulate the 3-D architecture and cellular organization of tumors than adherent cultures. However, it is not known whether they faithfully recapitulate the biophysics of the *in vivo* tumor microenvironment. To answer this question, we used our solid stress measurement method to compare solid stresses in spheroids and *in vivo* tumors (Fig. 7a). Since spheroids cannot be larger than 500 μm in diameter due to formation of necrosis[66], we only compared solid stresses measured at the cellular scale, and not at the tissue scale. Unexpectedly, we observed that the solid stresses in spheroids were not significantly different from those measured *in vivo* (Fig. 7b). Furthermore, we observed that cellular-scale solid stresses did not depend on the size of the spheroids, as determined by seeding density of the cancer cells (Fig. 7b). The similarities of solid stresses in spheroids, which were formed by cellular aggregation in 24-48 hours, and *in vivo* models, which were formed in a few days with stromal recruitment, implied that the cell-cell interactions played a major role in the genesis of solid stresses, and that the magnitude of solid stress was independent of the number of cells in the multi-cellular aggregates.

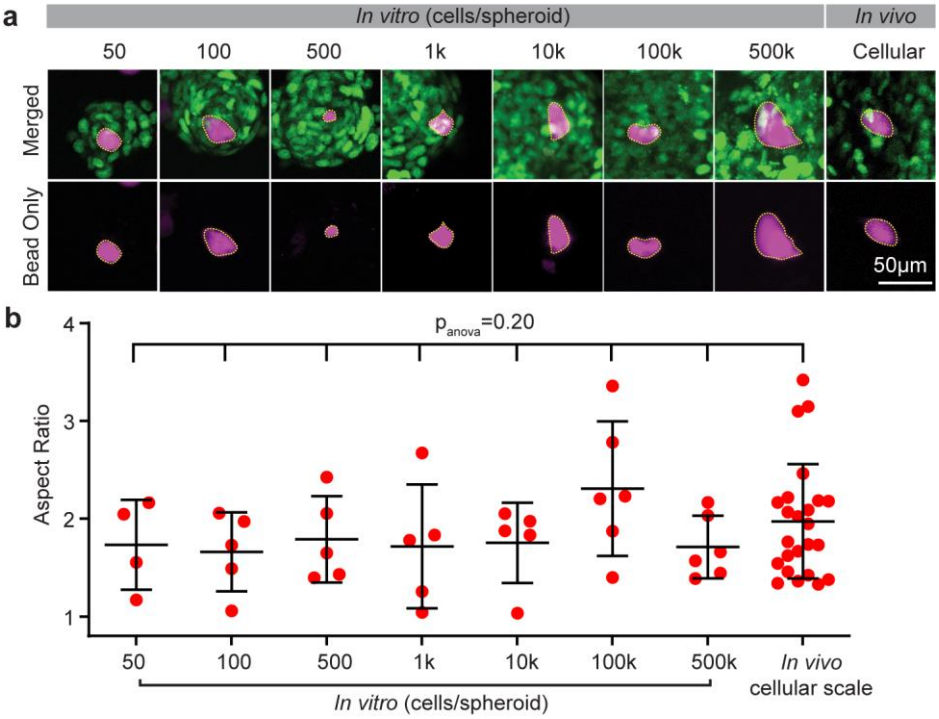

Figure 7| *In vitro* models of tumors faithfully model the solid stresses levels *in vivo* at the cellular scale. a, Representative images of spheroids at multiple seeding densities (2 days after seeding) and *in vivo* cellular scale (5 days after injection) (cancer cells (green), PA beads (magenta)). **b,** Aspect ratios of *in vitro* spheroids do not vary significantly by seeding density (mean ± STD, N=5-6 spheroids, one-way ANOVA, Tukey's multiple comparisons test) demonstrating the independence of solids stresses and the spheroid size. Aspect ratios of PA beads embedded in spheroids compared to *in vivo* cellular scale PA beads are not significantly different (mean ± STD, N=5 mice, n=24 beads, two-tailed Student's t-test) demonstrating that spheroid models recapitulate *in vivo* cellular-scale solid stresses.

Discussion

We report the first *in vivo* optical measurement of solid stresses in two mouse models of primary breast cancer and breast cancer lung metastasis. There are five key advantages of this method (i-v). (i) We demonstrate the longitudinal monitoring of the solid stress, as opposed to the terminal point measurements in existing methods[13,28,29], which is critical to characterize the role of solid stress in tumor progression and treatment response. Additionally, we confirm previous experimental studies showing that solid stress does not depend on interstitial fluid pressure[13] using a post-euthanasia model. (ii) Our *in vivo* method allows multi-scale measurement of the solid stresses. Previous methods report solid stresses in sub-millimeter resolution[28,29,34], while our methods estimates solid stresses at cellular and tissue scales, where tumors cells directly sense and respond to solid stress. This cellular-level capability enables the measurement of solid stress at early stages of tumorigenesis, e.g., when individual cells are arrested in the lung capillaries, or tumors as small as 100 μm

in diameter, a determination unachievable with existing low resolution methods[28,29]. (iii) Measurement of solid stress in small metastatic tumor is possible and allows the comparison of stresses in primary and metastatic tumors with important implications on the differential treatment response in primary vs metastatic tumors[58,67]. (iv) Our method affords a measurement of the full magnitude and direction of solid stresses. Previously developed *ex vivo* methods rely on a mechanical relaxation of the stress in the form of cutting or slicing the tumor[28,29], which relaxes solid stresses only partially in certain directions. In other works, fluorescent oil droplets were injected into mouse embryos to measure the anisotropic stresses within the tissue; however, oil droplets cannot be co-injected with cancer cells to induce primary and metastatic tumors, and due to the incompressibility of the oil droplets only anisotropic stresses can be measured[68,69]. With our method, the full solid stress, i.e., isotropic and anisotropic components, at a given point can be reported as a tensor, which provides both magnitude as well as direction of the stress components (Figure S12). (v) Finally, our method accounts for solid stress exerted by surrounding normal tissues, i.e., peritumoral solid stresses, since tumors are retained *in situ* and are not excised. In the previously reported *in situ* solid stress measurement method, accounting the solid stress exerted by surrounding tissues can cause solid stress measurements in the tumor to be a factor of 5 higher than the intratumoral stresses measured after the tumor has been excised[29].

Our *in vivo* characterization of solid stresses in breast tumors experimentally confirms that solid stress transmission is scale dependent, which has been predicted previously via mathematical modeling[41-43]. In a homogeneous material under uniform stress, it is expected that stresses at the cellular scale to be the same in magnitude to stresses at the tissue scale, as stress is normalized by length scale. In contrast, we observed that tumor cells experience ~5-8 times lower solid stresses at the cellular scale compared to the tissue scale. Given the immense biological and immunological implications of this finding with regards to the transmission of intratumoral solid stresses to tumors and immune cells, we tested and confirmed lack of biases in our experimental parameters through multiple approaches. First, in addition to stresses, we report elastic energy density and aspect ratio of the deformed beads, which are both normalized to the scale of the bead. In both readouts, we observe consistently larger solid stresses at the tissue scale compared to cell scale. Second, since the cellular level and tissue level measurements are performed in different experiments and mice, potential biases due to multi-cohort experiments are eliminated by measuring the solid stresses in a heterogeneous population of bead sizes (28.7 ± 18.2 μm) in the same mouse. Solid stresses deform large beads at a higher magnitude compared to smaller beads, consistent to the scale-dependence we observed in the much larger PA beads. The discerned scale-dependence in small vs large cell-sized beads in the same region of interest and using the same imaging modality (two-photon) further confirms our observation of increasing solid stress transmission with increasing PA bead size that we observed in cell- vs tissue-scale beads.

One of the key implications of the scale-dependence of solid stresses is the potential biophysical mechanism(s) that tumor cells utilize to protect themselves against the high solid stresses that exist at the tissue level. We show that growth-induced solid stresses generated at the tissue level can be as high as about ~6kPa (Fig. 3c), which is consistent with the previous measurements[29,30,35] but lower than previous measurements reported in tumor spheroids[32]. Such high mechanical stresses can be lethal to cells[37-39] given that the Young's modulus of individual cells is ~1kPa (Fig. 1h) and such high stresses would result in deformation of up to 50% of the cell diameter (Fig. 3d). Since the first measurement of solid stresses in tumors[13,29], the question of how tumor cells tolerate such high solid stress values has remained unanswered. Furthermore, recent studies show that solid stresses of ~0.1kPa damage and kill the cells in the normal tissue surrounding the tumor[21,22], which amplifies the dilemma on the differential response of tumor vs normal cell to solid stresses: if the compressive forces that tumors apply on normal tissue are equally felt by tumor cells, why do cells in the normal tissue succumb to solid stresses while tumor cells proliferate? A recently proposed biological mechanism to protect tumor cells against high levels of solid stress is the loss of p53 which enables neoplastic cells to be more resistant to high mechanical stress levels[5,37]. However, p53 is not universally mutated in all tumor cells, and such mechanical resistance phenotypes only apply to cancer cells with certain mutations and not to the intratumoral stromal cells without any mutation in p53. Therefore, we propose that the existence of biophysical mechanisms that dissipates the high macroscale solid stresses to much lower levels at the cellular scale could better explain how cancer cells, tumor-associated immune cells, fibroblasts, and blood vessels can tolerate solid stresses.

Another key implication of the solid stress scale-dependence is the differential compression of small vs large blood vessels in the tumors. Specifically, solid stresses compress the intratumoral[15,16,25,54,70] and extratumoral blood vessels[21], which fuels tumor progression and treatment resistance[71]. The scale-dependence of solid stress shows that large vessels, which could be mainly co-opted vessels, likely experience higher magnitudes of solid stress compared to capillaries and smaller vessels, which are more prone to collapse by compression due to lack of pericyte coverage[72]. As a result, this differential stress transmission to blood vessels bears important implications in vascular normalization and decompressing blood vessels by targeting solid stress[25,54,73-75].

While studying the origins of multi-scale transmission of solid stresses is beyond the scope of this study, we propose a hypothesis for the observed phenomena. To withstand high stresses within tumors, cancer and stromal cells may organize the ECM and cellular microarchitecture to generate stiffness heterogeneities at a certain characteristic length scale that dissipate the stresses at the cellular scale through a caging effect. In this proposed mechanism, the surrounding stiffer areas, acting collectively as a cage, protect the cells from excessive deformation. The proposed mechanism is supported by our findings that, in addition to solid stress transmission being larger at the tissue scale, the tissue scale reveals more heterogeneity in stress transmission that is not captured at the cellular scale, as shown by the larger range in stress magnitudes when FEM is performed on the original geometries of the deformed PA beads. This suggests that solid stress in the tumor is highly heterogeneous, yet cells do not experience the same level of heterogeneity. This supports our proposed mechanism that the caging effect reduces the magnitude of solid stress as well as the level of stress heterogeneity at the cellular scale. Due to the cell-size characteristic length scale of the stiffness heterogeneities, solid stresses compress and deform the tissue at the tissue level while cells experience smaller levels of solid stress. This caging effect may occur in tandem with tissues undergoing macroscale re-alignment to redistribute high mechanical stresses and thereby dissipate mechanical energy as proposed recently as a mechanism of nucleus protection[76]. Such adaptive caging effect is likely specific to the abnormal physical microenvironment in tumors that does not exist in normal tissue, which may explain why the normal tissue surrounding the tumors is more prone to damage compared to the tumor cells, despite experiencing similar levels of solid stresses at their interface[21]. Furthermore, our hypothesis is in accordance with previous studies which model scale-dependent stress in tissues[41-43]. These studies point to structural or material heterogeneities that give rise to differences in mechanical stress at the tissue vs cellular scale. Future studies in which the stiffness heterogeneities of the tumor can be characterized in 3-D and at the cellular resolution may provide more information to decipher the origin of this observation on the multiscale nature of the mechanical tumor microenvironment. Discovering the mechanism underlying the scale-dependence of solid stress transmission will also inform therapeutic strategies that disrupt the protective tumor microenvironment against solid stresses to increase the sensitivity of cancer cells to high stresses.

Using our method, we longitudinally measured stresses over 6 days, demonstrating the applicability of our method for observing stress with tumor growth and potential to be applied to understanding stress changes in response to cancer treatment in preclinical small animal models. We observed a rapid accumulation of stress over 2 days, which is also consistent with our *in vitro* measurement of solid stress. Our results reveal that metastatic tumors experience higher levels of stress intratumorally compared to primary tumors from the same cell. This different levels of solid stresses indicate the role of microenvironment in the genesis of solid stress, and may have implication on the differential treatment response observed between primary and metastatic tumors. This result also shows that cyclical breathing affects the stresses experienced by metastatic tumor cells. Furthermore, we confirm previous studies that show stress is anisotropic at the periphery of tumors and becomes more isotropic towards the core[13]. Our *in vivo* measurement method is also applicable to characterizing the solid stresses that cancer cells experience during metastasis, which can provide insight to the role of mechanical stress on the multistep metastatic cascade. The compression of individual cancer cells migrating through blood and lymphatic vessels affects their extravasation through the vasculature and their subsequent formation of micro- and macrometastasis[1,77]. The *in vivo* cellular-scale measurement of solid stresses is not limited to cancer cells; it is also amenable for studying the mechanosensitivity of immune cells, and provides an estimate of the solid stresses that immune cells experience as they circulate, sequester, and infiltrate into the lung microvasculature[60,78]. We also investigated whether solid stress measurement in metastatic sites could be extended to organs other than the lung. We imaged the liver and brain, which are two other common sites of metastasis, and surprisingly found compressed PA beads in the brain and liver

(Figure S18), demonstrating the applicability of our methods to study the physical tumor microenvironment in brain and liver metastasis *in vivo*.

Limitations of the intravital imaging of PA beads include: (i) being limited to measurements in small animal tumors in which an intravital window can be implanted, such as in the mammary fat pad, brain, liver, and lymph nodes[79,80], (ii) having a timeframe limited to under 2 weeks for longitudinal imaging, (iii) limited range of depth penetration intrinsic to light microscopy, and (iv) stochastic distribution of PA beads in tumors. (v) The imaging of deformations in PA beads is an indirect method for measuring stress, and (vi) PA bead diameters need to be known a priori to estimate the total stress, which includes both isotropic and anisotropic components. Furthermore, (vii) stress measurements in metastatic sites are limited to the cellular scale since the method relies on hematogenous delivery of PA beads and large beads result in fatal impediment of blood flow.

In summary, we report the first *in vivo* optical measurement of intratumoral solid stresses in the primary setting where the complexities of the tumor microenvironment are preserved. Our *in vivo* methods equip cancer researchers with a multi-scale tool to better understand the spatiotemporal co-evolution of the physics, biology, and immunology of cancer. The discoveries that solid stress transmission is scale-dependent and that individual cancer cells experience substantially lower solid stresses than experienced at the macroscale provide important insights for mechano-adaption in tumors. Furthermore, we show that stresses in the metastatic setting are higher than that of the primary setting. These findings will pave the way for discovering new biophysical mechanisms that cancer and stromal cells utilize to protect themselves against lethally high solid stresses and for novel treatments that alter the solid stresses in the tumor or increase tumor cell sensitivity to solid stresses.

Methods

Polyacrylamide formulation, fabrication, and functionalization

The fabrication of PA beads was performed using water-in-oil stirred emulsion polymerization as previously described[45]. Polyacrylamide (PA) formulations were prepared to achieve the following Young's modulus (E) by altering the percentages of acrylamide (40% stock, Bio-rad, 1610140) and bisacrylamide (2% stock, Bio-rad, 1610142): E=0.215 ± 0.042 kPa (3% acrylamide, 0.06% bisacrylamide), E=0.38± 0.15 kPa (5% acrylamide, 0.03% bisacrylamide), 0.49 ± 0.1 kPa (4% acrylamide, 0.03% bisacrylamide)[81]. PA pre-polymer solutions were prepared in rubber-sealed glass vials and purged with nitrogen gas (N_2) for 15 minutes. The oil phase, kerosene (Sigma-Aldrich, 329460) with 6% w/v PGPR 4150 surfactant (Palsgaard, 90415001) was prepared in an Erlenmeyer flask and purged with N2 for 30 min. To 1 mL of pre-polymer mixture, 10 µL of 10% w/v methacryloxyethyl thiocarbamoyl rhodamine B (Polysciences, 23591-100) or fluorescein O-methacrylate (Sigma, 568864) in dimethyl sulfoxide (DMSO) was added, followed by 100 µL of 1% w/v ammonium persulfate (APS; Bio-rad, 1610700) in phosphate buffered saline (PBS) and 5 µL of tetramethylethylenediamine (TEMED; Sigma-Aldrich, T7024).

The pre-polymer solution was injected into the oil phase and the emulsion was vortexed for 10s. The emulsion was magnetically stirred at 300-600 rpm (300rpm for tissue-scale beads and 600-700rpm for cellular-scale beads) for 60 minutes while the beads polymerized. The beads were centrifuged to remove the kerosene with surfactant and subsequently cleaned with kerosene to remove remaining surfactant. The beads were recovered in PBS through multiple centrifugation steps.

Beads were filtered to tissue-scale (397 ± 69 µm in diameter) or cellular-scale (28.7 ± 18.2 µm) sizes using stainless steel wire cloth (McMaster) fitted to custom-designed filter holders. The beads were then sterilized under UV light for 15 minutes and swelled overnight in PBS at 4°C. Beads were resuspended in 0.05 mg/mL Sulfo-SANPAH (G-Biosciences, BC38) in PBS and irradiated under UV light for 4 min to activate the cross-linker. Beads were rinsed with PBS, and resuspended and incubated overnight in 40 µg/mL fibronectin (Sigma Aldrich, F1141) to allow for cell adhesion and promote uptake of beads by the tumor. The fibronectin-treated beads were resuspended in PBS and stored at 4°C in low adhesion microcentrifuge tubes to prevent beads from adhering to the tube. Fibronectin-treated beads are fluorescent and cell-adherent for at least 1 year after fabrication when stored in isotonic PBS at 4°C.

Cell culture

The MCa-M3C HER2/neu+ with H2B-labelled dendra2 (*Her2*+, *p53*+) cell line (MCa-M3C-H2B-dendra2, gift from Rakesh Jain, Ph.D.) is a highly metastatic HER2/neu+ mammary tumor line derived from the MMTV-PyVT/FVB transgenic mouse[46,70,82]. The E0771 with H2B-labelled dendra2 cell line (E0771-H2B-dendra2, gift from Rakesh Jain, Ph.D.) is derived from a spontaneous mammary tumor in C57BL/6 mice. Cells were cultured in Dulbecco's Modified Eagle's medium with L-Glutamine, 4.5g/L Glucose and Sodium Pyruvate (DMEM; Corning) supplemented with 10% fetal bovine serum (FBS; Fisher Scientific, SH3039603) and 1% antibiotic-antimycotic (Fisher Scientific, 15240062) at 37 °C and 5% CO_2. Cells were harvested at ~80% confluency, counted, and resuspended in DMEM. All cell lines repeatedly tested negative for mycoplasma using the Mycoalert Plus Mycoplasma Detection Kit (Lonza, Allendale, NJ).

Culture of beads in spheroids for *in vitro* measurements of solid stress

Spheroids were cultured in 96-well Clear Round Bottom Ultra-Low Attachment Microplates (Corning, 7007) with 500 to 500,000 cells per well in 200µL of cell culture media to form spheroids of different sizes. Between 1-10 fibronectin-functionalized beads were seeded per well in accordance to the number of cells seeded per spheroid. More beads were seeded for larger spheroids in order to increase the probability that a bead would end up at a depth in the spheroid that could be imaged via confocal microscopy. The plate was centrifuged at 1200 rpm for 10 minutes to coalesce the cells and beads. The spheroids were cultured at 37 °C and 5% CO_2 for 24 to 48 hours. As cells coalesce to form spheroids, beads become embedded within the spheroid and may end up anywhere from the core to the edge of the spheroid.

Animal Models

All animal procedures were approved by the Institutional Animal Care and Use Committee of Boston University. A breeding pair of transgenic B6.129(Cg)-Gt(ROSA)26Sortm4(ACTB-tdTomato,-EGFP)Luo/J (JAX #007676)[83], hereafter referred to as mTmG, was purchased from JAX to start a colony and was used in select *ex vivo* lung experiments. mTmG mice aged 6-14 weeks were used for experiments. C57BL/6 and FVB/NJ female mice aged 6-8 weeks were purchased from (JAX). All mice were housed and bred under pathogen-free conditions at the Boston University Animal Science Center. All animal experience conformed to ethical principles and guidelines under protocols approved by the Boston University Institutional Animal Care and Use Committee.

Primary breast tumor model for *in vivo* measurements of solid stress

Tumors were formed either via injection into the mammary fat pad under intact skin or injection under the intravital window into the mammary fat pad. Approximately 10 (tissue-scale: 397 ± 69 µm in diameter) or 500 (cellular-scale: 28.7 ± 18.2 µm) fibronectin-functionalized beads and $1x10^6$ MCa-M3C-H2B-dendra2 cells[46] (*Her2*+) or E0771-H2B-dendra cells in 50 µL of DMEM were co-injected into the mammary fat pad of 6-8 week old female FVB/NJ mice (JAX) for MCa-M3C-H2B-dendra2 tumors and C57BL/6 mice (JAX) for E0771-H2B-dendra tumors. The same batches of tissue-scale and cellular-scale beads were used throughout all mammary tumor experiments. Tumors were grown for 5-7 days and resulted in a palpable mass when cancer cells were injected under the skin (Figure S13). For tumors grown via injection under the window, an upright stereomicroscope (Nikon) with a GFP filter and blue light excitation (NightSea) was used to confirm presence of fluorescent mass under the window. Tumors were size-matched for cellular- and tissue-scale experiments (tumor dimensions: ~3x3mm^2 to 6x6mm^2).

Tumor induction under intravital mammary window for *in vivo* measurements of solid stress

Multiple methods of tumor induction under the window were investigated. Injecting cancer cells and PA beads directly under the window with and without Matrigel did not result in formation of tumors. Stereotactic injection of the cancer cells and PA beads under a thin layer of tissue under the window resulted in formation of tumors, as confirmed using a fluorescent stereomicroscope. While injection of Matrigel directly under the window did not form tumors, it did allow for enough contrast for visualization of tissue-scale beads at day 0 of injection (Figure S14). For future experiments, injection of Matrigel

with cancer cells and beads can be performed stereotactically under a thin layer of tissue for tracking of tumor formation from day 0 at the tissue scale.

Lung, liver and brain models for *ex vivo* measurements of solid stress

Approximately 10,000 cellular-scale rhodamine-labelled, fibronectin-functionalized microbeads and 1.5x106 MCa-M3C-H2B-dendra2 were co-injected via tail-vein into 6-8 week old female FVB/NJ mice (JAX). Lung metastases between ~100 μm to 2mm in diameter formed ~1-2 weeks after injection; large metastatic nodules were identified via a fluorescent stereomicroscope. The same lung with metastases had non-tumor and tumor regions. Non-tumor regions were defined as regions of the lung without any cancer cells present on the tissue surface within a 500 μm radius. Fluorescein-labelled cellular-scale fibronectin-functionalized microbeads, which had Young's moduli of 0.49 ± 0.1 kPa, were injected into mTmG mice for analysis of stress experienced by single cancer cells in the lung, liver and

Implantation of window

The Royal Blue SFA Stereo Microscope Fluorescence Adapter (NightSea) was used to visualize fluorescence under the skin to determine the presence of a tumor. The skin was removed from the tumor and custom-designed, 3D-printed intravital imaging windows (Clear Resin, Formlabs; Figure S1) were sutured over the mammary fat pad. A 10 mm diameter round coverslip (#1.5 0.16-0.19mm, Ted Pella) was placed onto the window and secured using a metal retaining ring (91580A132, McMaster). For tumors formed after intravital window implantation, $1x10^6$ MCa-M3C-H2B-dendra2 cells were injected as a bolus under a thin layer of tissue under the window. A custom-fitted stainless-steel cover was fabricated to protect the window from mouse chewing.

Lung, liver, and brain extraction and imaging

Prior to sacrifice in FVB mice, 50 μL of Cascade Blue dextran (10 kDa) (Fisher) was co-injected intracardiac at 10 mg/mL with 100 μL of 1.25 mg/mL heparin sulfate and allowed to circulate for 3 minutes before animal sacrifice to distribute the dye and heparin[84]. Mice were anesthetized with a ketamine/xylazine cocktail (100 and 10 mg/kg, respectively) injected intraperitoneally and ventilated through a tracheal cannula. The mouse was then sacrificed via exsanguination, ensuring that the lungs did not collapse but maintained an alveolar pressure of 5 cmH_2O. The skin, fascia, and intercostal muscles, and ribs were dissected away under a stereomicroscope (Nikon) till the underlying lung-heart bloc was visible. The lungs were then removed from the ribcage and placed into a transparent polystyrene crystal ribcage for imaging, as previously reported[65]. A tube connected to the trachea cannula was used to inflate the lung with room air to various defined pressures using a water column. The pleural surface of the lung was imaged through the crystal ribcage with upright two photon microscopy (Bruker) using a 16x water immersion objective, or confocal microscope (Olympus FV3000, Fluoview software) to identify metastatic nodules and PA beads at the surface of the lung using a 10x objective, with environmental temperature set to 37°C. The liver and brain were harvested from mTmG mice 3 hours after injection of PA beads. The dorsal surface of the brain and the anterior surface of the liver were imaged under confocal microscopy. Microscopy data was visualized using FIJI and MATLAB2022b. Quantification of bead aspect ratio in lung images were measured as a maximum projection of the 3D stack in the XY direction.

Imaging with fluorescent stereomicroscope

The Royal Blue SFA Stereo Microscope Fluorescence Adapter (NightSea) was used with an upright stereomicroscope (Nikon) to visualize tumors above 1mm in diameter.

Confocal imaging for *in vitro* measurements of solid stress in tumor spheroids

In vitro spheroid images were acquired using the Olympus FV3000 laser scanning confocal microscope using either a UPLSAPO10X2 (Olympus, NA 0.4, 10x magnification) or LUCPLFLN20X (Olympus, NA 0.45, 20x magnification) air immersion objective lens (Olympus) at scanning resolutions between 512x512 and 1024x1024 pixels in FV31S-SW Viewer software (Olympus). MCa-M3C-H2B-dendra2 cells were imaged using a 488nm laser excitation and a 525/60 nm variable barrier filter. Rhodamine-labelled polyacrylamide beads were imaged using a 561nm laser excitation and a 600/50 variable barrier filter (Olympus).

Intravital imaging

Inhalation of isoflurane (1.5-2% vol/vol, 0.1-0.5L/min, Kent Scientific 0-1 LPM VetFlo system) was used to anesthetize the animal during imaging. An intravital mammary window was implanted for 2-photon or OCT imaging and the intravital window was immobilized by an in-house fabricated stage (Figure S1). 2-photon imaging was used for imaging cellular-scale PA beads, and OCT was used to image tissue-scale PA beads. The glass coverslip on the intravital window was removed for imaging when tumors were formed prior to window implantation to prevent artificial compression of the tumor during imaging. Imaging was performed approximately 5-7 days after cancer cell injection, unless otherwise noted.

Two-photon (2P) microscopy system

2P images were taken with a 16x water immersion objective lens (16X Nikon CFI LWD Plan Fluorite Objective, 0.08 NA) using the Bruker Investigator system, which consists of an Insight X3 laser (Spectra Physics). The system has a 700 nm short-pass primary dichroic with an IR blocker (Chroma) in the detection path. A filter cube with 595/50 nm and 525/70 nm filters (Chroma) and a 565 nm long-pass secondary dichroic (Chroma) were used to image fluorescently-labelled cells and beads and lung autofluorescence. Samples were excited with 880 nm using a laser power of approximately 50 mW at the sample plane. Images were taken at scanning resolutions between 512x512 to 1024x1024 pixels with 1-3x digital zoom using galvo scanning without averaging. PrairieView software (Bruker) was used for 2P imaging.

Optical coherence tomography system

We used a commercial spectral-domain OCT system (Telesto TEL320C1, Thorlabs, New Jersey) and ThorImage OCT software (Thorlabs). The light source is a broadband superluminescent diode with center wavelength of 1300 nm and a full width half maximum bandwidth of 150 nm, yielding an axial resolution of 4.2 μm in tissue. The spectrometer has a 2048-pixel InGaAs line scan camera operating at an A-line rate of 76 kHz. The total imaging depth is 2.6 mm in tissue. A 10X air objective (Mitutoyo, 0.28 NA) was used in the sample arm, which yields a lateral resolution of 3.5 μm with a theoretical Rayleigh range of 40 μm in a nonscattering medium. The maximum sensitivity of the system is 109 dB.

Euthanasia

Euthanasia was performed by intraperitoneal (IP) injecting 150mg/kg of Euthasol (Virbac) for primary tumor experiments.

Collagenase/hyaluronidase treatment for tumor dissociation

Collagenase/hyaluronidase enzyme solution was prepared by dissolving 100mg collagenase from *Clostridium histolyticum* (Sigma, C0130), 50mg hyaluronidase from bovine testes (Sigma, H3506), and 2mg $CaCl_2$ in 30 mL DMEM. The coverslip from the intravital window was removed and we applied the enzyme solution to animals post-euthanasia to comply with our animal protocols. The tumors were imaged before and after euthanasia (before the application of enzyme) to control for potential effects on euthanasia on solid stress. For tissue-scale experiments, the enzyme solution was applied to the tumor without excision and incubated at 37 °C for 180 minutes using a thermostatic heating pad. For cellular-scale experiments, tumors were excised and placed in the enzyme solution at 37 °C.

Trypsin treatment for spheroid dissociation

The media from individual wells of spheroids cultured in 96-well plates was removed and the spheroids were washed twice with PBS in the wells to remove serum proteins. Trypsin-EDTA (0.05%) (Gibco) was added to each spheroid in the 96-well plate and the spheroids were incubated for 24 hours in trypsin-EDTA at 37°C to fully dissociate the cells.

Histology of tumor sections

Tumors were resected and fixed with 4% paraformaldehyde overnight, washed with PBS, and cryoprotected with 15% sucrose for 6-12 hours, followed by 30% sucrose overnight. The tumors were embedded in a cryostat embedding medium, flash frozen, and cryosectioned into 10 μm slices. Tissue sections were stained with hematoxylin and eosin. Slides were imaged using the Olympus VS120 Virtual Slide Scanner.

Quantification of solid stress

The quantification of solid stress was performed in a multi-step approach (Figure S17). First, 3-D image stacks were segmented following one of two methods: in the first method, the deformed PA bead geometry is approximated to an ellipsoid to allow for a relatively more high-throughput, semi-automated analysis; in the second method, the irregular deformed geometry of the PA bead is retained through manual segmentation of the bead boundary and allows for more complex analysis of solid stress with geometric irregularities. In both methods, point-clouds are generated which represent either the ellipsoidal approximation of the deformed bead or retains the original deformed bead geometry, depending on the method used. Subsequently, the point-clouds are used to determine the surface displacement field of the deformed bead from the undeformed bead. For quantification of solid stress in which the deformed bead was relaxed to its undeformed, approximately spherical geometry via the enzymatic dissociation of cellular components, the undeformed bead was approximated to a sphere and the diameter of the sphere was taken as the undeformed bead diameter. For images of beads in which the tissue was not enzymatically dissociated, the undeformed bead was assumed to be spherical, with a diameter equal to the longest axis length of the ellipsoidal approximation of the deformed bead. This approximation is justified in Figure S10. The surface displacement field is written into an input file that is interpreted by ABAQUS (Dassault Systèmes) as displacement boundary conditions determining the x-, y-, z-displacements of each node in the finite element model.

3-D image segmentation

Multiple regions of interest (ROI) were imaged per mouse, and multiple beads in each ROI were analyzed. Beads which did not have distinct boundaries due to close proximity to other beads were excluded from analysis. The built-in MATLAB Image Processing Toolbox (Mathworks) function, *imadjustn*, was used to increase the contrast of the bead to background in the volumetric image by saturating the top 1% and bottom 1% of all pixel values. For confocal and two-photon 3-D image stacks, the built-in function *drawrectangle* was used to manually isolate individual beads to generate smaller 3-D stacks. Image stacks of tissue-scale PA beads obtained by OCT were manually segmented in MATLAB using the built-in *drawfreehand* function by drawing outlines around the boundary of the bead throughout the 3-D stack (Figure S11). Manual segmentation was also used for confocal and two-photon 3-D images stacks when retaining the irregular geometry was necessary for complex solid stress analysis. To account for resolution differences in the x-, y- and z-dimensions before image segmentation in all cases, the image pixels were up-sampled in the z-dimension in MATLAB by a factor of *x,y resolution / z resolution*.

Ellipsoid fitting for solid stress approximation

Ray tracing originating at the geometric centroid of the image was used to determine the pixel intensity profiles along a set of rays iterating through all integer values for ϕ and Θ of the polar coordinate axes. Intensity profiles of the pixels were then fit to a sigmoidal curve of the form,

$$a + ((b + c(x - d))/(1 + exp(e * (x - d)))) \quad (1)$$

where *x* is the distance radially outward from the geometric centroid of the image stack. Variable parameters *a, b, c, d,* and *e* for ray profiles were optimized through least-squares fitting using the Levenberg-Marquardt algorithm. The boundary of the PA bead was estimated to be where the sigmoidal function reached 50% of the maximum intensity of all pixels. The pixels within the boundary of the PA bead were represented as a 3-D point-cloud. Intensity profiles that could not be fit using the least-squares algorithm were discarded, but were at a low enough occurrence (~1-5% of total rays) that they did not affect the overall resolution of the point-cloud approximation.

Following image segmentation, the 3-D point-cloud of the PA bead was down-sampled to prevent over-fitting in the subsequent ellipsoid fitting algorithm. The point-cloud was down-sampled first as a function of ϕ (ϕ = 5:25, 155:180, reduction in points by 6x; ϕ = 30:50, 130:150, reduction in points by 4x; ϕ = 55:125, reduction in points by 2x) and then by a further 40%, so that 60% of the points after initial down-sampling are used in the downstream ellipsoid fitting process. In the creation of the analysis pipeline, 10 simulations were run for down-sampling values from 10% to 90% in increments of 10%. When the residual distance between each boundary point and the closest face of the ellipsoid was calculated and normalized by the total number of points used in that fit, a 40% reduction showed the best balance between fit accuracy (as represented by a low normalized residual distance) and a low variation in fit accuracy across multiple samples. Down-sampled point-clouds were fit to an affine invariant 3-D ellipsoid using a Douglas-Rachford iterative algorithm with singular value[85]. Ellipsoid axis lengths and centers were calculated from the modeled 3-D surface map. The ratio of the largest to smallest axis length of the ellipsoid fit was taken as the aspect ratio of the polyacrylamide bead. A step-by-step visualization of the process can be found in Figure S11.

Mathematical and finite element modelling

The stress-free, undeformed state of the PA bead, which was assumed to be a sphere, was generated in ABAQUS (Dassault Systèmes) using element type C3D10, a quadratic axisymmetric tetrahedral element, with 4899 elements and 7425 surface nodes. The surface node positions were input into a custom, semi-automated MATLAB code to determine the displacement field of the surface of the deformed bead from the surface of the undeformed, spherical bead. The centroid of the point-cloud representing the approximation or actual geometry of the deformed PA bead was aligned to the spherical point-cloud representation of the undeformed bead determined by finding the position of the bead which resulted in the lowest surface strain energy,

$$Surface\ strain\ energy = \frac{1}{2}k\sum_{i}^{N} {x_i}^2 \quad (2)$$

where x_i is the distance between the deformed and undeformed bead at node i, k is the spring constant of the PA bead, and N is the total number of nodes on the surface of the undeformed bead. For ellipsoidal approximations of the deformed PA bead, the centroid of the deformed point-cloud was aligned to the centroid of the undeformed bead since this positioning results in the lowest total surface strain energy and the undeformed bead diameter was estimated as the longest axis length of the deformed bead (see justification in Figure S10). For point-clouds that are generated from manually segmented beads, the position of the deformed bead centroid was shifted in an iterative, stepwise manner in x-, y-, and z-directions to calculate the total surface strain energy which would result at each position. The centroid position resulting in the lowest total surface strain energy was used to determine the surface displacement boundary conditions. The displacement boundary conditions were quantified by generating rays extending outwards from the centroid of the deformed bead to a node on the undeformed bead point cloud. A ray triangulation algorithm[86] was used to generate a node position at the intersection between the ray and the surface of the deformed bead. The distance between the node on the deformed bead and the corresponding node on the undeformed bead was used to quantify the x-, y-, and z-displacement boundary conditions.

An axisymmetric finite element code was developed in ABAQUS to translate the displacement boundary conditions representing the stress-induced deformation of PA beads to solid stress. We used element type C3D10, a quadratic axisymmetric tetrahedral element to mesh the undeformed and deformed beads in ABAQUS. A quasi-static condition was used with non-linear geometry enabled. We defined a hyperelastic material, with test stress/strain data from the indentation of a cylindrical polyacrylamide hydrogel, obtained using an Instron 5900 Series System. The test data was fit using Ogden 3rd order hyperelastic model in ABAQUS, with a Poisson's ratio of 0.22. The Poisson's ratio was determined experimentally by measuring the axial and lateral strain resulting from compressing a bulk polyacrylamide hydrogel in an unconfined compression test[87], and was measured as 0.22 ± 0.028. A linear stress/strain curve representing constant Young's modulus was fit to the first point of the

nonlinear stress/strain curve (Figure S6). The slope of the linear stress/strain curve was determined by average Young's modulus values of cellular- and tissue-scale beads, obtained via AFM as described in Methods. The Young's modulus was separately determined by AFM for each batch of beads fabricated. The average of the Young's modulus was used in the ABAQUS model and the Young's modulus was assumed to be homogeneous throughout the bead. The density of the polyacrylamide bead was assumed to be 1.3 g/cm^3 as reported in literature[88]. The average of the absolute values of minimum principal stresses are reported, as solid stresses are mainly compressive[32,89], and reported as <|Principal stress|> for simplification. The recoverable strain energy output by ABAQUS was divided by the volume of the ABAQUS model to obtain the total elastic energy density. The elastic energy density is given by the function,

$$Elastic\ energy\ density\ (W) = \frac{1}{2V}\int_V \sigma_{ij}\varepsilon_{ij}dV \quad (3)$$

where σ_{ij} is the stress tensor, ε_{ij} is the strain tensor, and V is the volume of the ABAQUS sphere.

AFM-based measurement of indentation modulus

The indentation moduli of polyacrylamide beads, single cells, spheroids and tumor samples were measured using Igor AFM software (v16, Asylum Resarch) on the Asylum MFP-3D Bio System (Asylum Research, Santa Barbara, CA) with an Olympus IX71 Inverted Microscope. Polyacrylamide beads were immobilized on plasma-treated glass slides. Spheroids were immobilized on Cell-Tak treated glass slides. Cells were grown on glass coverslips to approximately 70% confluence. Tumors were resected, cut in half, and immobilized on glass slides using cyanoacrylate glue. We used polystyrene colloidal probe tips with end radius R ~ 15 μm (Polysciences, Warrington, PA) attached to tipless cantilevers with nominal spring constant k ~ 0.2 N/m (Bruker, Camarillo, CA). Using the AFM system, the colloidal probes were attached to the cantilever by the following process: a dot of glue (Hernon Ultrabond 721) was applied onto a tipless cantilever by making quick contact between the cantilever and a thin layer of glue (1 μl) spread over a glass surface and then immediate contact was made between the tip of the cantilever and a colloid probe resting on a glass slide for 1 min with the cantilever pushing against the colloid. This process was followed by UV curing for 30 seconds. For each probe tip, the exact spring constants of the cantilevers were directly measured using the thermal calibration method[90]. The relationship between the detected voltage and the applied force was calibrated by bringing the cantilever in contact with a glass slide and calculating the slope of the voltage-displacement curve. The displacement, d, was translated to force, F, using Hooke's Law (F = kd). The indentation was performed under a force control scheme (max force ~20nN), limiting the indentation depths to 0.5–3 μm. The tip displacement was obtained by subtracting the cantilever deflection from vertical movement of the piezo. An indentation approach velocity of 2 μm/s ensured probing the elastic modulus close to equilibrium condition.

The effective indentation modulus E_{ind} was computed using Hertzian contact mechanics models via least-squares linear regression of the experimental loading force-displacement curves. For the spherical colloidal probe tip with end radius R_1 on a PA bead sample with radius R_2 (here, R_2 ~ 50-500 μm, R_1~ 15 μm),

$$F = \frac{4}{3}E_{ind}\left(\frac{R_1R_2}{R_1+R_2}\right)^{\frac{1}{2}} * \frac{(d_{total})^{\frac{3}{2}}}{1+\left(\frac{R_1}{R_1+R_2}\right)^{\frac{1}{3}}} \quad (4)$$

where F is the indentation force and d_{total} is the indentation depth. A representative force-displacement curve is shown in Fig. 1h.

For tumor samples which are much thicker compared to the colloidal probe tip radius R_1, E_{ind} was computed using

$$F = \frac{4}{3}\frac{E_{ind}}{(1-\nu^2)}R^{\frac{1}{2}} * (d_{total})^{\frac{3}{2}} \quad (5)$$

where R is the radius of the spherical colloidal probe tip and v is the Poisson's ratio of the tumor sample, which was assumed to be 0.2[63,91,92].

A modified Hertz model for bonded, thin samples was used to calculate the E_{ind} in single cells[93]:

$$F = \frac{16E_{ind}}{9} R^{\frac{1}{2}} (d_{total})^{\frac{3}{2}} * [1 + 1.133\chi + 1.283\chi^2 + 0.769\chi^3 + 0.0975\chi^4] \quad (6)$$

$$\chi = \sqrt{\frac{R * d_{total}}{h}} \quad (7)$$

where R is the radius of the colloidal probe tip (R=20μm) and h is the height of the cell (h=8μm).

The stress relaxation time constant was determined

Statistical analysis

Groups were compared using an unpaired, two-tailed Student's t-test (due to independent sampling) or one-way ANOVA followed by Tukey's multiple comparisons test. Paired two-tailed Wilcoxon matched-pairs signed rank t-test was performed for experiments where the same PA bead could be tracked. The Pearson correlation coefficient, r, was quantified to determine the strength of linear association between two variables.

Reporting Summary. Further information on research design is available in the Nature Research Reporting Summary linked to this article.

Availability of biological materials. The cell lines used in this study are available for research purposes on reasonable request.

Data availability. The main data supporting the results in this study are available within the paper and its Supplementary Information. The raw and analyzed datasets generated during the study are too large to be publicly shared, yet they are available for research purposes from the corresponding authors on reasonable request.

Code availability. MATLAB codes are available at: https://github.com/suezhangBU/solid_stress.

References

1 Nia, H. T., Munn, L. L. & Jain, R. K. Physical traits of cancer. *Science* **370** (2020). https://doi.org:10.1126/science.aaz0868

2 Kechagia, J. Z., Ivaska, J. & Roca-Cusachs, P. Integrins as biomechanical sensors of the microenvironment. *Nat Rev Mol Cell Biol* **20**, 457-473 (2019). https://doi.org:10.1038/s41580-019-0134-2

3 Benham-Pyle, B. W., Pruitt, B. L. & Nelson, W. J. Mechanical strain induces E-cadherin-dependent Yap1 and beta-catenin activation to drive cell cycle entry. *Science* **348**, 1024-1027 (2015). https://doi.org:10.1126/science.aaa4559

4 Munn, L. L. & Nia, H. T. Mechanosensing tensile solid stresses. *Proc Natl Acad Sci U S A* **116**, 21960-21962 (2019). https://doi.org:10.1073/pnas.1916115116

5 Levayer, R. Solid stress, competition for space and cancer: The opposing roles of mechanical cell competition in tumour initiation and growth. *Semin Cancer Biol* **63**, 69-80 (2020). https://doi.org:10.1016/j.semcancer.2019.05.004

6 Smith, M. L., Gourdon, D., Little, W. C., Kubow, K. E., Eguiluz, R. A., Luna-Morris, S. & Vogel, V. Force-induced unfolding of fibronectin in the extracellular matrix of living cells. *PLoS Biol* **5**, e268 (2007). https://doi.org:10.1371/journal.pbio.0050268

7 Saini, K., Cho, S., Dooling, L. J. & Discher, D. E. Tension in fibrils suppresses their enzymatic degradation - A molecular mechanism for 'use it or lose it'. *Matrix Biol* **85-86**, 34-46 (2020). https://doi.org:10.1016/j.matbio.2019.06.001

8 Kubow, K. E., Vukmirovic, R., Zhe, L., Klotzsch, E., Smith, M. L., Gourdon, D., Luna, S. & Vogel, V. Mechanical forces regulate the interactions of fibronectin and collagen I in extracellular matrix. *Nat Commun* **6**, 8026 (2015). https://doi.org:10.1038/ncomms9026

9 Kirby, T. J. & Lammerding, J. Emerging views of the nucleus as a cellular mechanosensor. *Nat Cell Biol* **20**, 373-381 (2018). https://doi.org:10.1038/s41556-018-0038-y

10 Cho, S., Irianto, J. & Discher, D. E. Mechanosensing by the nucleus: From pathways to scaling relationships. *J Cell Biol* **216**, 305-315 (2017). https://doi.org:10.1083/jcb.201610042

11 Chauhan, V. P., Martin, J. D., Liu, H., Lacorre, D. A., Jain, S. R., Kozin, S. V., Stylianopoulos, T., Mousa, A. S., Han, X., Adstamongkonkul, P., Popovic, Z., Huang, P., Bawendi, M. G., Boucher, Y. & Jain, R. K. Angiotensin inhibition enhances drug delivery and potentiates chemotherapy by decompressing tumour blood vessels. *Nat Commun* **4**, 2516 (2013). https://doi.org:10.1038/ncomms3516

12 Padera, T. P., Stoll, B. R., Tooredman, J. B., Capen, D., di Tomaso, E. & Jain, R. K. Cancer cells compress intratumour vessels. *Nature* **427**, 695 (2004). https://doi.org:10.1038/427695a

13 Stylianopoulos, T., Martin, J. D., Chauhan, V. P., Jain, S. R., Diop-Frimpong, B., Bardeesy, N., Smith, B. L., Ferrone, C. R., Hornicek, F. J., Boucher, Y., Munn, L. L. & Jain, R. K. Causes, consequences, and remedies for growth-induced solid stress in murine and human tumors. *Proc Natl Acad Sci U S A* **109**, 15101-15108 (2012). https://doi.org:10.1073/pnas.1213353109

14 Mpekris, F., Panagi, M., Voutouri, C., Martin, J. D., Samuel, R., Takahashi, S., Gotohda, N., Suzuki, T., Papageorgis, P., Demetriou, P., Pierides, C., Koumas, L., Costeas, P., Kojima, M., Ishii, G., Constantinidou, A., Kataoka, K., Cabral, H. & Stylianopoulos, T. Normalizing the Microenvironment Overcomes Vessel Compression and Resistance to Nano-immunotherapy in Breast Cancer Lung Metastasis. *Adv Sci (Weinh)* **8**, 2001917 (2021). https://doi.org:10.1002/advs.202001917

15 Jain, R. K. Antiangiogenesis strategies revisited: from starving tumors to alleviating hypoxia. *Cancer Cell* **26**, 605-622 (2014). https://doi.org:10.1016/j.ccell.2014.10.006

16 Munn, L. L. & Jain, R. K. Vascular regulation of antitumor immunity. *Science* **365**, 544-545 (2019). https://doi.org:10.1126/science.aaw7875

17 Jones, D., Wang, Z., Chen, I. X., Zhang, S., Banerji, R., Lei, P. J., Zhou, H., Xiao, V., Kwong, C., van Wijnbergen, J. W. M., Pereira, E. R., Vakoc, B. J., Huang, P., Nia, H. T. & Padera, T. P. Solid stress impairs lymphocyte infiltration into lymph-node metastases. *Nat Biomed Eng* **5**, 1426-1436 (2021). https://doi.org:10.1038/s41551-021-00766-1

18 Tse, J. M., Cheng, G., Tyrrell, J. A., Wilcox-Adelman, S. A., Boucher, Y., Jain, R. K. & Munn, L. L. Mechanical compression drives cancer cells toward invasive phenotype. *Proc Natl Acad Sci U S A* **109**, 911-916 (2012). https://doi.org:10.1073/pnas.1118910109

19 Das, J. & Maiti, T. K. in *Autophagy in tumor and tumor microenvironment* Ch. Chapter 8, 171-182 (2020).

20 Fernandez-Sanchez, M. E., Barbier, S., Whitehead, J., Bealle, G., Michel, A., Latorre-Ossa, H., Rey, C., Fouassier, L., Claperon, A., Brulle, L., Girard, E., Servant, N., Rio-Frio, T., Marie, H., Lesieur, S., Housset, C., Gennisson, J. L., Tanter, M., Menager, C., Fre, S., Robine, S. & Farge, E. Mechanical induction of the tumorigenic beta-catenin pathway by tumour growth pressure. *Nature* **523**, 92-95 (2015). https://doi.org:10.1038/nature14329

21 Seano, G., Nia, H. T., Emblem, K. E., Datta, M., Ren, J., Krishnan, S., Kloepper, J., Pinho, M. C., Ho, W. W., Ghosh, M., Askoxylakis, V., Ferraro, G. B., Riedemann, L., Gerstner, E. R., Batchelor, T. T., Wen, P. Y., Lin, N. U., Grodzinsky, A. J., Fukumura, D., Huang, P., Baish, J. W., Padera, T. P., Munn, L. L. & Jain, R. K. Solid stress in brain tumours causes neuronal loss and neurological dysfunction and can be reversed by lithium. *Nat Biomed Eng* **3**, 230-245 (2019). https://doi.org:10.1038/s41551-018-0334-7

22 Nia, H. T., Datta, M., Seano, G., Zhang, S., Ho, W. W., Roberge, S., Huang, P., Munn, L. L. & Jain, R. K. In vivo compression and imaging in mouse brain to measure the effects of solid stress. *Nat Protoc* **15**, 2321-2340 (2020). https://doi.org:10.1038/s41596-020-0328-2

23 Panagi, M., Mpekris, F., Chen, P., Voutouri, C., Nakagawa, Y., Martin, J. D., Hiroi, T., Hashimoto, H., Demetriou, P., Pierides, C., Samuel, R., Stylianou, A., Michael, C., Fukushima, S., Georgiou, P., Papageorgis, P., Papaphilippou, P. C., Koumas, L., Costeas, P., Ishii, G., Kojima, M., Kataoka, K., Cabral, H. & Stylianopoulos, T. Polymeric micelles effectively reprogram the tumor microenvironment to potentiate nano-immunotherapy in mouse breast cancer models. *Nat Commun* **13**, 7165 (2022). https://doi.org:10.1038/s41467-022-34744-1

24 Provenzano, P. P., Cuevas, C., Chang, A. E., Goel, V. K., Von Hoff, D. D. & Hingorani, S. R. Enzymatic targeting of the stroma ablates physical barriers to treatment of pancreatic ductal adenocarcinoma. *Cancer Cell* **21**, 418-429 (2012). https://doi.org:10.1016/j.ccr.2012.01.007

25 Zhao, Y., Cao, J., Melamed, A., Worley, M., Gockley, A., Jones, D., Nia, H. T., Zhang, Y., Stylianopoulos, T., Kumar, A. S., Mpekris, F., Datta, M., Sun, Y., Wu, L., Gao, X., Yeku, O., Del Carmen, M. G., Spriggs, D. R., Jain, R. K. & Xu, L. Losartan treatment enhances chemotherapy

efficacy and reduces ascites in ovarian cancer models by normalizing the tumor stroma. *Proc Natl Acad Sci U S A* **116**, 2210-2219 (2019). https://doi.org:10.1073/pnas.1818357116

26 ClinicalTrials.Gov: Proton w/FOLFIRINOX-Losartan for Pancreatic Cancer; Identifier NCT01821729.

27 Murphy, J. E., Wo, J. Y., Ryan, D. P., Clark, J. W., Jiang, W., Yeap, B. Y., Drapek, L. C., Ly, L., Baglini, C. V., Blaszkowsky, L. S., Ferrone, C. R., Parikh, A. R., Weekes, C. D., Nipp, R. D., Kwak, E. L., Allen, J. N., Corcoran, R. B., Ting, D. T., Faris, J. E., Zhu, A. X., Goyal, L., Berger, D. L., Qadan, M., Lillemoe, K. D., Talele, N., Jain, R. K., DeLaney, T. F., Duda, D. G., Boucher, Y., Fernandez-Del Castillo, C. & Hong, T. S. Total Neoadjuvant Therapy With FOLFIRINOX in Combination With Losartan Followed by Chemoradiotherapy for Locally Advanced Pancreatic Cancer: A Phase 2 Clinical Trial. *JAMA Oncol* **5**, 1020-1027 (2019). https://doi.org:10.1001/jamaoncol.2019.0892

28 Nia, H. T., Datta, M., Seano, G., Huang, P., Munn, L. L. & Jain, R. K. Quantifying solid stress and elastic energy from excised or in situ tumors. *Nat Protoc* **13**, 1091-1105 (2018). https://doi.org:10.1038/nprot.2018.020

29 Nia, H. T., Liu, H., Seano, G., Datta, M., Jones, D., Rahbari, N., Incio, J., Chauhan, V. P., Jung, K., Martin, J. D., Askoxylakis, V., Padera, T. P., Fukumura, D., Boucher, Y., Hornicek, F. J., Grodzinsky, A. J., Baish, J. W., Munn, L. L. & Jain, R. K. Solid stress and elastic energy as measures of tumour mechanopathology. *Nat Biomed Eng* **1** (2016). https://doi.org:10.1038/s41551-016-0004

30 Voutouri, C., Mpekris, F., Papageorgis, P., Odysseos, A. D. & Stylianopoulos, T. Role of constitutive behavior and tumor-host mechanical interactions in the state of stress and growth of solid tumors. *PLoS One* **9**, e104717 (2014). https://doi.org:10.1371/journal.pone.0104717

31 Dolega, M. E., Delarue, M., Ingremeau, F., Prost, J., Delon, A. & Cappello, G. Cell-like pressure sensors reveal increase of mechanical stress towards the core of multicellular spheroids under compression. *Nat Commun* **8**, 14056 (2017). https://doi.org:10.1038/ncomms14056

32 Helmlinger, G., Netti, P. A., Lichtenbeld, H. C., Melder, R. J. & Jain, R. K. Solid stress inhibits the growth of multicellular tumor spheroids. *Nat Biotechnol* **15**, 778-783 (1997). https://doi.org:10.1038/nbt0897-778

33 Shah, M. K., Leary, E. A. & Darling, E. M. Integration of hyper-compliant microparticles into a 3D melanoma tumor model. *J Biomech* **82**, 46-53 (2019). https://doi.org:10.1016/j.jbiomech.2018.10.018

34 Islam, M. T., Tasciotti, E. & Righetti, R. Non-Invasive Imaging of Normalized Solid Stress in Cancers in Vivo. *IEEE J Transl Eng Health Med* **7**, 4300209 (2019). https://doi.org:10.1109/JTEHM.2019.2932059

35 Islam, M. T. & Righetti, R. A New Poroelastography Method to Assess the Solid Stress Distribution in Cancers. *IEEE Access* **7**, 103404-103415 (2019). https://doi.org:10.1109/access.2019.2929021

36 Islam, M. T. & Righetti, R. A Novel Finite Element Model to Assess the Effect of Solid Stress Inside Tumors on Elastographic Normal Strains and Fluid Pressure. *J Eng Sci Med Diagnostics Ther* **2** (2019). https://doi.org:doi:10.1115/1.4044048

37 Wagstaff, L., Goschorska, M., Kozyrska, K., Duclos, G., Kucinski, I., Chessel, A., Hampton-O'Neil, L., Bradshaw, C. R., Allen, G. E., Rawlins, E. L., Silberzan, P., Carazo Salas, R. E. & Piddini, E. Mechanical cell competition kills cells via induction of lethal p53 levels. *Nat Commun* **7**, 11373 (2016). https://doi.org:10.1038/ncomms11373

38 Takao, S., Taya, M. & Chiew, C. Mechanical stress-induced cell death in breast cancer cells. *Biol Open* **8** (2019). https://doi.org:10.1242/bio.043133

39 Matamoro-Vidal, A. & Levayer, R. Multiple Influences of Mechanical Forces on Cell Competition. *Curr Biol* **29**, R762-R774 (2019). https://doi.org:10.1016/j.cub.2019.06.030

40 McGrail, D. J., McAndrews, K. M., Brandenburg, C. P., Ravikumar, N., Kieu, Q. M. & Dawson, M. R. Osmotic Regulation Is Required for Cancer Cell Survival under Solid Stress. *Biophys J* **109**, 1334-1337 (2015). https://doi.org:10.1016/j.bpj.2015.07.046

41 Hepworth, D. G., Steven-fountain, A., Bruce, D. M. & Vincent, J. F. Affine versus non-affine deformation in soft biological tissues, measured by the reorientation and stretching of collagen fibres through the thickness of compressed porcine skin. *J Biomech* **34**, 341-346 (2001). https://doi.org:10.1016/s0021-9290(00)00183-4

42 Guilak, F. & Mow, V. C. The mechanical environment of the chondrocyte: a biphasic finite element model of cell-matrix interactions in articular cartilage. *J Biomech* **33**, 1663-1673 (2000).

43 Chan, V. W. L., Tobin, W. R., Zhang, S., Winkelstein, B. A., Barocas, V. H., Shephard, M. S. & Picu, C. R. Image-based multi-scale mechanical analysis of strain amplification in neurons embedded in collagen gel. *Comput Methods Biomech Biomed Engin* **22**, 113-129 (2019). https://doi.org:10.1080/10255842.2018.1538414

44 Girardo, S., Traber, N., Wagner, K., Cojoc, G., Herold, C., Goswami, R., Schlussler, R., Abuhattum, S., Taubenberger, A., Reichel, F., Mokbel, D., Herbig, M., Schurmann, M., Muller, P., Heida, T., Jacobi, A., Ulbricht, E., Thiele, J., Werner, C. & Guck, J. Standardized microgel beads as elastic cell mechanical probes. *J Mater Chem B* **6**, 6245-6261 (2018). https://doi.org:10.1039/c8tb01421c

45 Lee, W., Kalashnikov, N., Mok, S., Halaoui, R., Kuzmin, E., Putnam, A. J., Takayama, S., Park, M., McCaffrey, L., Zhao, R., Leask, R. L. & Moraes, C. Dispersible hydrogel force sensors reveal patterns of solid mechanical stress in multicellular spheroid cultures. *Nat Commun* **10**, 144 (2019). https://doi.org:10.1038/s41467-018-07967-4

46 Li, W., Li, S., Chen, I. X., Liu, Y., Ramjiawan, R. R., Leung, C. H., Gerweck, L. E., Fukumura, D., Loeffler, J. S., Jain, R. K., Duda, D. G. & Huang, P. Combining losartan with radiotherapy increases tumor control and inhibits lung metastases from a HER2/neu-positive orthotopic breast cancer model. *Radiat Oncol* **16**, 48 (2021). https://doi.org:10.1186/s13014-021-01775-9

47 Borriello, L., Condeelis, J., Entenberg, D. & Oktay, M. H. Breast Cancer Cell Re-Dissemination from Lung Metastases-A Mechanism for Enhancing Metastatic Burden. *J Clin Med* **10** (2021). https://doi.org:10.3390/jcm10112340

48 Traber, N., Uhlmann, K., Girardo, S., Kesavan, G., Wagner, K., Friedrichs, J., Goswami, R., Bai, K., Brand, M., Werner, C., Balzani, D. & Guck, J. Polyacrylamide Bead Sensors for in vivo Quantification of Cell-Scale Stress in Zebrafish Development. *Sci Rep* **9**, 17031 (2019). https://doi.org:10.1038/s41598-019-53425-6

49 Boudou, T., Ohayon, J., Picart, C., Pettigrew, R. I. & Tracqui, P. Nonlinear elastic properties of polyacrylamide gels: implications for quantification of cellular forces. *Biorheology* **46**, 191-205 (2009). https://doi.org:10.3233/BIR-2009-0540

50 Islam, M. T., Tang, S., Liverani, C., Saha, S., Tasciotti, E. & Righetti, R. Non-invasive imaging of Young's modulus and Poisson's ratio in cancers in vivo. *Sci Rep* **10**, 7266 (2020). https://doi.org:10.1038/s41598-020-64162-6

51 Stylianopoulos, T. & Jain, R. K. Combining two strategies to improve perfusion and drug delivery in solid tumors. *Proc Natl Acad Sci U S A* **110**, 18632-18637 (2013). https://doi.org:10.1073/pnas.1318415110

52 Jacobetz, M. A., Chan, D. S., Neesse, A., Bapiro, T. E., Cook, N., Frese, K. K., Feig, C., Nakagawa, T., Caldwell, M. E., Zecchini, H. I., Lolkema, M. P., Jiang, P., Kultti, A., Thompson, C. B., Maneval, D. C., Jodrell, D. I., Frost, G. I., Shepard, H. M., Skepper, J. N. & Tuveson, D. A. Hyaluronan impairs vascular function and drug delivery in a mouse model of pancreatic cancer. *Gut* **62**, 112-120 (2013). https://doi.org:10.1136/gutjnl-2012-302529

53 Islam, M. T., Tang, S. & Righetti, R. Non-Invasive Assessment of the Spatial and Temporal Distributions of Interstitial Fluid Pressure, Fluid Velocity and Fluid Flow in Cancers in Vivo. *IEEE Access*, 89222-89233 (2021). https://doi.org:10.1109/ACCESS.2021.3089454

54 Chauhan, V. P., Boucher, Y., Ferrone, C. R., Roberge, S., Martin, J. D., Stylianopoulos, T., Bardeesy, N., DePinho, R. A., Padera, T. P., Munn, L. L. & Jain, R. K. Compression of pancreatic tumor blood vessels by hyaluronan is caused by solid stress and not interstitial fluid pressure. *Cancer Cell* **26**, 14-15 (2014). https://doi.org:10.1016/j.ccr.2014.06.003

55 Boucher, Y., Baxter, L. T. & Jain, R. K. Interstitial pressure gradients in tissue-isolated and subcutaneous tumors: implications for therapy. *Cancer Res* **50**, 4478-4484 (1990).

56 Zanetti-Dallenbach, R., Plodinec, M., Oertle, P., Redling, K., Obermann, E. C., Lim, R. Y. H. & Schoenenberger, C. A. Length Scale Matters: Real-Time Elastography versus Nanomechanical Profiling by Atomic Force Microscopy for the Diagnosis of Breast Lesions. *Biomed Res Int* **2018**, 3840597 (2018). https://doi.org:10.1155/2018/3840597

57 Plodinec, M., Loparic, M., Monnier, C. A., Obermann, E. C., Zanetti-Dallenbach, R., Oertle, P., Hyotyla, J. T., Aebi, U., Bentires-Alj, M., Lim, R. Y. & Schoenenberger, C. A. The nanomechanical signature of breast cancer. *Nat Nanotechnol* **7**, 757-765 (2012). https://doi.org:10.1038/nnano.2012.167

58 Padera, T. P., Kuo, A. H., Hoshida, T., Liao, S., Lobo, J., Kozak, K. R., Fukumura, D. & Jain, R. K. Differential response of primary tumor versus lymphatic metastasis to VEGFR-2 and VEGFR-3 kinase inhibitors cediranib and vandetanib. *Mol Cancer Ther* **7**, 2272-2279 (2008). https://doi.org:10.1158/1535-7163.MCT-08-0182

59 Labriola, N. R., Mathiowitz, E. & Darling, E. M. Fabricating polyacrylamide microbeads by inverse emulsification to mimic the size and elasticity of living cells. *Biomater Sci* **5**, 41-45 (2016). https://doi.org:10.1039/c6bm00692b

60 Solis, A. G., Bielecki, P., Steach, H. R., Sharma, L., Harman, C. C. D., Yun, S., de Zoete, M. R., Warnock, J. N., To, S. D. F., York, A. G., Mack, M., Schwartz, M. A., Dela Cruz, C. S., Palm, N. W., Jackson, R. & Flavell, R. A. Mechanosensation of cyclical force by PIEZO1 is essential for innate immunity. *Nature* **573**, 69-74 (2019). https://doi.org:10.1038/s41586-019-1485-8

61 Maruyama, K., Nemoto, E. & Yamada, S. Mechanical regulation of macrophage function - cyclic tensile force inhibits NLRP3 inflammasome-dependent IL-1beta secretion in murine macrophages. *Inflamm Regen* **39**, 3 (2019). https://doi.org:10.1186/s41232-019-0092-2

62 Li, C., Hu, Y., Mayr, M. & Xu, Q. Cyclic strain stress-induced mitogen-activated protein kinase (MAPK) phosphatase 1 expression in vascular smooth muscle cells is regulated by Ras/Rac-MAPK pathways. *J Biol Chem* **274**, 25273-25280 (1999). https://doi.org:10.1074/jbc.274.36.25273

63 Stylianopoulos, T., Martin, J. D., Snuderl, M., Mpekris, F., Jain, S. R. & Jain, R. K. Coevolution of solid stress and interstitial fluid pressure in tumors during progression: implications for vascular collapse. *Cancer Res* **73**, 3833-3841 (2013). https://doi.org:10.1158/0008-5472.CAN-12-4521
64 Limjunyawong, N., Fallica, J., Horton, M. R. & Mitzner, W. Measurement of the pressure-volume curve in mouse lungs. *J Vis Exp*, 52376 (2015). https://doi.org:10.3791/52376
65 Banerji, R., Grifno, G. N., Shi, L., Smolen, D., LeBourdais, R., Muhvich, J., Eberman, C., Hiller, B., Lee, J., Regan, K., Zheng, S., Zhang, S. S., Jiang, J., Phil, R., Traber, K., Ligresti, G., Mizgerd, J. P., Suki, B. & Nia, H. T. Probing lung function at high spatiotemporal resolution using a novel crystal ribcage. (2022). https://doi.org:10.1101/2022.10.28.514251
66 Vinci, M., Gowan, S., Boxall, F., Patterson, L., Zimmermann, M., Court, W., Lomas, C., Mendiola, M., Hardisson, D. & Eccles, S. A. Advances in establishment and analysis of three-dimensional tumor spheroid-based functional assays for target validation and drug evaluation. *BMC Biol* **10**, 29 (2012). https://doi.org:10.1186/1741-7007-10-29
67 Kodack, D. P., Askoxylakis, V., Ferraro, G. B., Sheng, Q., Badeaux, M., Goel, S., Qi, X., Shankaraiah, R., Cao, Z. A., Ramjiawan, R. R., Bezwada, D., Patel, B., Song, Y., Costa, C., Naxerova, K., Wong, C. S. F., Kloepper, J., Das, R., Tam, A., Tanboon, J., Duda, D. G., Miller, C. R., Siegel, M. B., Anders, C. K., Sanders, M., Estrada, M. V., Schlegel, R., Arteaga, C. L., Brachtel, E., Huang, A., Fukumura, D., Engelman, J. A. & Jain, R. K. The brain microenvironment mediates resistance in luminal breast cancer to PI3K inhibition through HER3 activation. *Sci Transl Med* **9** (2017). https://doi.org:10.1126/scitranslmed.aal4682
68 Campas, O., Mammoto, T., Hasso, S., Sperling, R. A., O'Connell, D., Bischof, A. G., Maas, R., Weitz, D. A., Mahadevan, L. & Ingber, D. E. Quantifying cell-generated mechanical forces within living embryonic tissues. *Nat Methods* **11**, 183-189 (2014). https://doi.org:10.1038/nmeth.2761
69 Gross, B., Shelton, E., Gomez, C. & Campàs, O. STRESS, an automated geometrical characterization of deformable particles for in vivo measurements of cell and tissue mechanical stresses. (2021). https://doi.org:10.1101/2021.03.26.437148
70 Chauhan, V. P., Chen, I. X., Tong, R., Ng, M. R., Martin, J. D., Naxerova, K., Wu, M. W., Huang, P., Boucher, Y., Kohane, D. S., Langer, R. & Jain, R. K. Reprogramming the microenvironment with tumor-selective angiotensin blockers enhances cancer immunotherapy. *Proc Natl Acad Sci U S A* **116**, 10674-10680 (2019). https://doi.org:10.1073/pnas.1819889116
71 Martin, J. D., Seano, G. & Jain, R. K. Normalizing Function of Tumor Vessels: Progress, Opportunities, and Challenges. *Annu Rev Physiol* **81**, 505-534 (2019). https://doi.org:10.1146/annurev-physiol-020518-114700
72 Cleaver, O. & Melton, D. A. Endothelial signaling during development. *Nat Med* **9**, 661-668 (2003). https://doi.org:10.1038/nm0603-661
73 Jain, R. K. Normalizing tumor microenvironment to treat cancer: bench to bedside to biomarkers. *J Clin Oncol* **31**, 2205-2218 (2013). https://doi.org:10.1200/JCO.2012.46.3653
74 Jain, R. K. Normalization of tumor vasculature: an emerging concept in antiangiogenic therapy. *Science* **307**, 58-62 (2005). https://doi.org:10.1126/science.1104819
75 Stylianopoulos, T., Munn, L. L. & Jain, R. K. Reengineering the Physical Microenvironment of Tumors to Improve Drug Delivery and Efficacy: From Mathematical Modeling to Bench to Bedside. *Trends Cancer* **4**, 292-319 (2018). https://doi.org:10.1016/j.trecan.2018.02.005
76 Nava, M. M., Miroshnikova, Y. A., Biggs, L. C., Whitefield, D. B., Metge, F., Boucas, J., Vihinen, H., Jokitalo, E., Li, X., Garcia Arcos, J. M., Hoffmann, B., Merkel, R., Niessen, C. M., Dahl, K. N. & Wickstrom, S. A. Heterochromatin-Driven Nuclear Softening Protects the Genome against Mechanical Stress-Induced Damage. *Cell* **181**, 800-817 e822 (2020). https://doi.org:10.1016/j.cell.2020.03.052
77 Wirtz, D., Konstantopoulos, K. & Searson, P. C. The physics of cancer: the role of physical interactions and mechanical forces in metastasis. *Nat Rev Cancer* **11**, 512-522 (2011). https://doi.org:10.1038/nrc3080
78 Lefrancais, E., Ortiz-Munoz, G., Caudrillier, A., Mallavia, B., Liu, F., Sayah, D. M., Thornton, E. E., Headley, M. B., David, T., Coughlin, S. R., Krummel, M. F., Leavitt, A. D., Passegue, E. & Looney, M. R. The lung is a site of platelet biogenesis and a reservoir for haematopoietic progenitors. *Nature* **544**, 105-109 (2017). https://doi.org:10.1038/nature21706
79 Kedrin, D., Gligorijevic, B., Wyckoff, J., Verkhusha, V. V., Condeelis, J., Segall, J. E. & van Rheenen, J. Intravital imaging of metastatic behavior through a mammary imaging window. *Nat Methods* **5**, 1019-1021 (2008). https://doi.org:10.1038/nmeth.1269
80 Pittet, M. J. & Weissleder, R. Intravital imaging. *Cell* **147**, 983-991 (2011). https://doi.org:10.1016/j.cell.2011.11.004
81 Tse, J. R. & Engler, A. J. Preparation of hydrogel substrates with tunable mechanical properties. *Curr Protoc Cell Biol* **Chapter 10**, Unit 10 16 (2010). https://doi.org:10.1002/0471143030.cb1016s47
82 Chen, I. X., Chauhan, V. P., Posada, J., Ng, M. R., Wu, M. W., Adstamongkonkul, P., Huang, P., Lindeman, N., Langer, R. & Jain, R. K. Blocking CXCR4 alleviates desmoplasia, increases T-

lymphocyte infiltration, and improves immunotherapy in metastatic breast cancer. *Proc Natl Acad Sci U S A* **116**, 4558-4566 (2019). https://doi.org:10.1073/pnas.1815515116
83 Muzumdar, M. D., Tasic, B., Miyamichi, K., Li, L. & Luo, L. A global double-fluorescent Cre reporter mouse. *Genesis* **45**, 593-605 (2007). https://doi.org:10.1002/dvg.20335
84 Vanderpool, R. R. & Chesler, N. C. Characterization of the isolated, ventilated, and instrumented mouse lung perfused with pulsatile flow. *J Vis Exp* (2011). https://doi.org:10.3791/2690
85 Kovac, B., Fehrenbach, J., Guillaume, L. & Weiss, P. FitEllipsoid: a fast supervised ellipsoid segmentation plugin. *BMC Bioinformatics* **20**, 142 (2019). https://doi.org:10.1186/s12859-019-2673-0
86 Moller, T. A Fast Triangle-Triangle Intersection Test. *J Graph Tools* **2**, 25-30 (1997). https://doi.org:doi:10.1080/10867651.1997.10487472
87 Danso, E. K., Julkunen, P. & Korhonen, R. K. Poisson's ratio of bovine meniscus determined combining unconfined and confined compression. *J Biomech* **77**, 233-237 (2018). https://doi.org:10.1016/j.jbiomech.2018.07.001
88 Tarasova, N., Zanin, A., Krivoborodov, E., Toropygin, I., Pascal, E. & Mezhuev, Y. The New Approach to the Preparation of Polyacrylamide-Based Hydrogels: Initiation of Polymerization of Acrylamide with 1,3-Dimethylimidazolium (Phosphonooxy-)Oligosulphanide under Drying Aqueous Solutions. *Polymers (Basel)* **13** (2021). https://doi.org:10.3390/polym13111806
89 Cheng, G., Tse, J., Jain, R. K. & Munn, L. L. Micro-environmental mechanical stress controls tumor spheroid size and morphology by suppressing proliferation and inducing apoptosis in cancer cells. *PLoS One* **4**, e4632 (2009). https://doi.org:10.1371/journal.pone.0004632
90 Hutter, J. L. & Bechhoefer, J. Calibration of atomic-force microscope tips. *Review of Scientific Instruments* **64**, 1868-1873 (1993). https://doi.org:10.1063/1.1143970
91 Roose, T., Netti, P. A., Munn, L. L., Boucher, Y. & Jain, R. K. Solid stress generated by spheroid growth estimated using a linear poroelasticity model. *Microvasc Res* **66**, 204-212 (2003). https://doi.org:10.1016/s0026-2862(03)00057-8
92 Netti, P. A., Berk, D. A., Swartz, M. A., Grodzinsky, A. J. & Jain, R. K. Role of extracellular matrix assembly in interstitial transport in solid tumors. *Cancer Res* **60**, 2497-2503 (2000).
93 Dimitriadis, E. K., Horkay, F., Maresca, J., Kachar, B. & Chadwick, R. S. Determination of elastic moduli of thin layers of soft material using the atomic force microscope. *Biophys J* **82**, 2798-2810 (2002). https://doi.org:10.1016/S0006-3495(02)75620-8

Acknowledgements. We thank the Neurophotonics Center at Boston University for their generous support and access to their facility. Research reported in this publication was supported by the Boston University Micro and Nano Imaging Facility and the Office of the Director, National Institutes of Health of the National Institutes of Health under award Number S10OD024993. The content is solely the responsibility of the authors and does not necessarily represent the official views of the National Institute of Health.

Funding. H.T.N. discloses support for the research described in this study from the National Institutes of Health [DP2HL168562 and R21EB031332], Beckman Young Investigator Award, Boston University Center for Multiscale and Translational Mechanobiology, and the American Cancer Society Institutional Fund at Boston University.

Author contributions

S.Z. and H.T.N. conceived the project and wrote the manuscript; S.Z. conducted most of the experiments, performed data analysis and generated the experimental mice; R.P. assisted with collecting and analyzing spheroid data; K.R. generated the image segmentation and ellipsoid-fitting codes; M.H. collected Young's modulus data of cells, spheroids and tumors with AFM; G.G. generated lung metastasis models and performed lung extraction and imaging; S.Y.Z. collected mechanical data on polyacrylamide hydrogels; L.O. assisted with the design and fabrication of the intravital window and imaging stage; V.C. assisted with polyacrylamide bead fabrication; S.Y.K. assisted with generating code for defining bead deformations; J.Y. assisted with optical coherence tomography imaging; R.B. provided materials for lung imaging; L.S. performed liver and brain experiments, K.K, D.R. and M.W.G. contributed to discussions on crucial aspects of the project; H.T.N. supervised the project and provided guidance on experimental design, data interpretation and writing of the manuscript.

Competing interests

The authors declare no competing interests.

Supplementary Figures

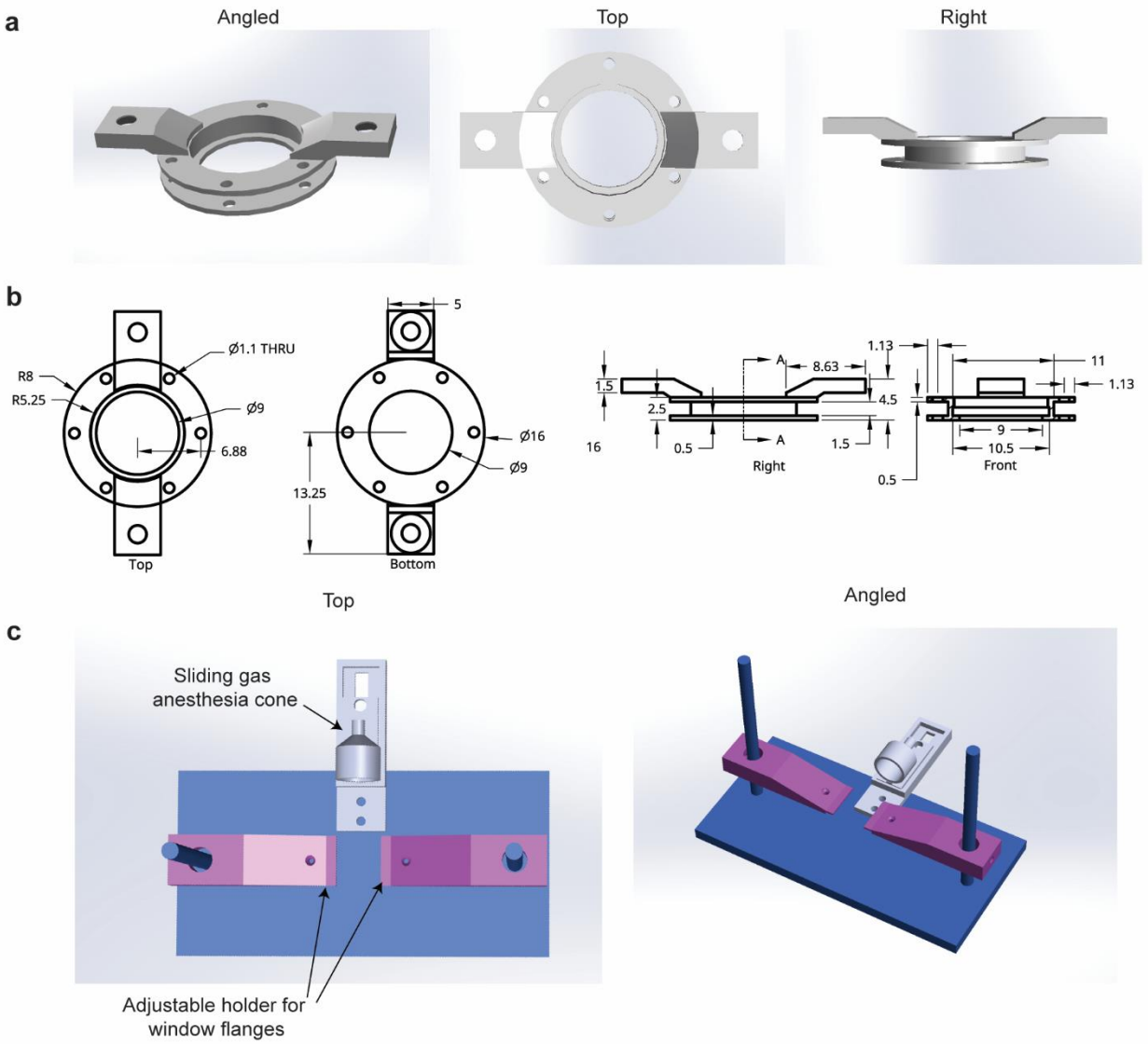

Figure S1| The design and fabrication of custom-made imaging window chamber and imaging stage. **a,** Angled, top, and right-side views of the 3-D printed imaging window. **b,** Dimensions of imaging window chamber (dimensions in mm) **c,** Top and angled view of imaging stage.

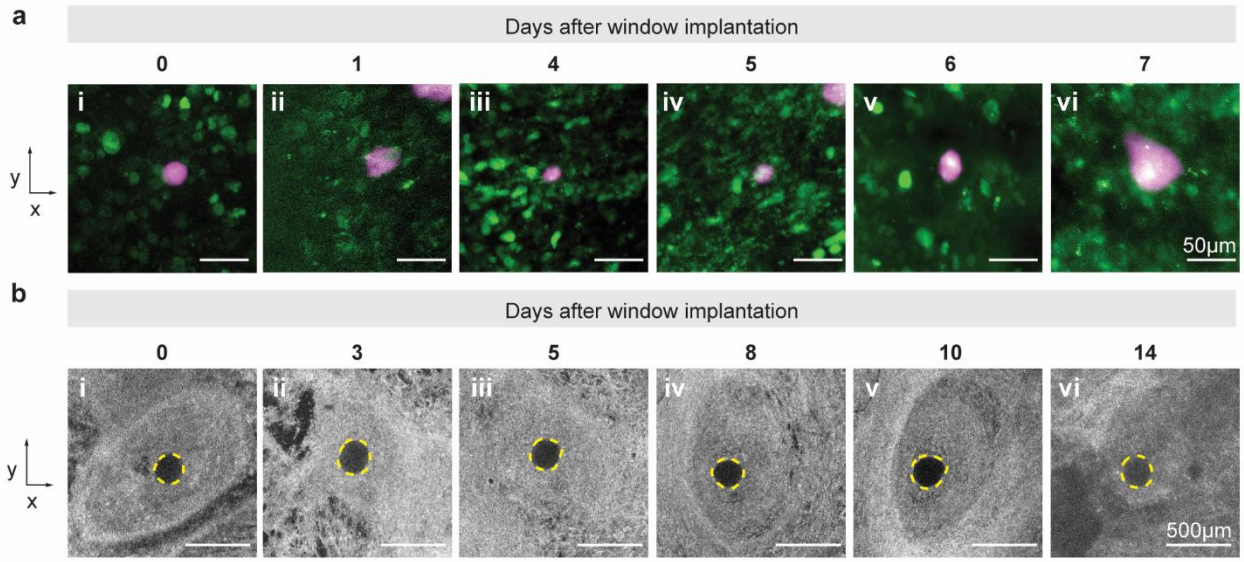

Figure S2| Longitudinal *in vivo* imaging of MCa-M3C-H2B-dendra2 tumors at the cellular and tissue scale. a, Cellular-scale beads (0.77 ± 0.16 kPa) were imaged up to 7 days via two-photon microscopy (cancer cells (green), PA beads (magenta)) and **b,** tissue-scale beads (E= 1.3 ± 0.13 kPa) were tracked up to 14 days via optical coherence microscopy (PA bead (outlined in yellow)).

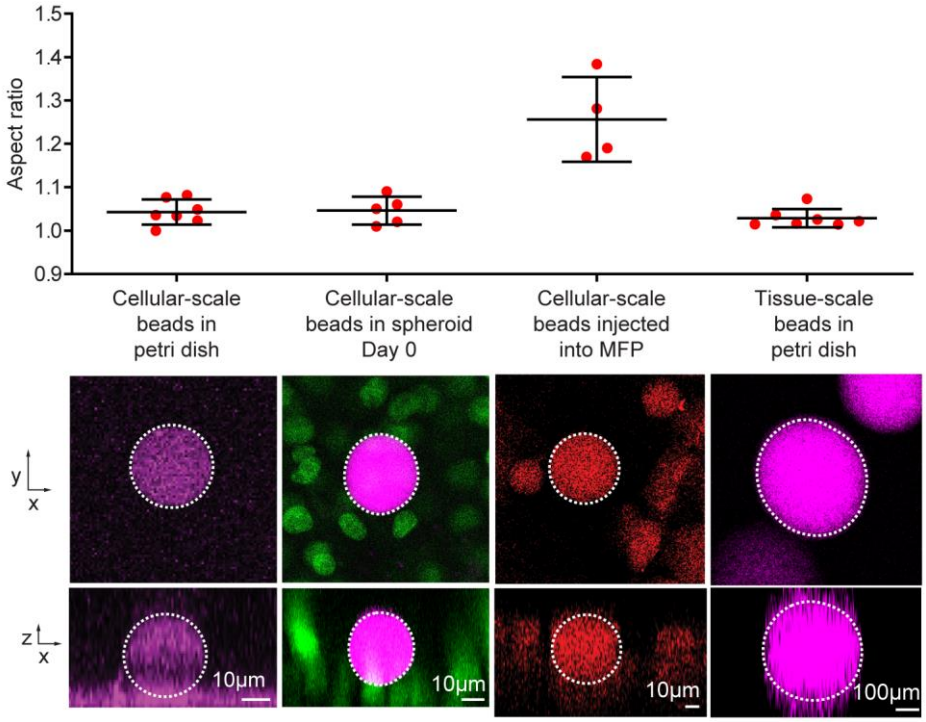

Figure S3| Injection through needle does not result in deformation in cellular- and tissue-scale beads. **a,** Measurement of bead aspect ratios after injecting through 25G (cellular scale) and 22G (tissue scale) needles into petri dish are close to 1 (mean ± STD, n=4-7 beads)**. b,** Bead after injecting through needle, XY and XZ views (bead (dotted white outline)). **c,** Bead after injecting into mammary fat pad of mouse without any tumor (bead (dotted white outline)). The lack of any distinct deformation demonstrates that the PA beads were not deformed prior to the development of the tumor.

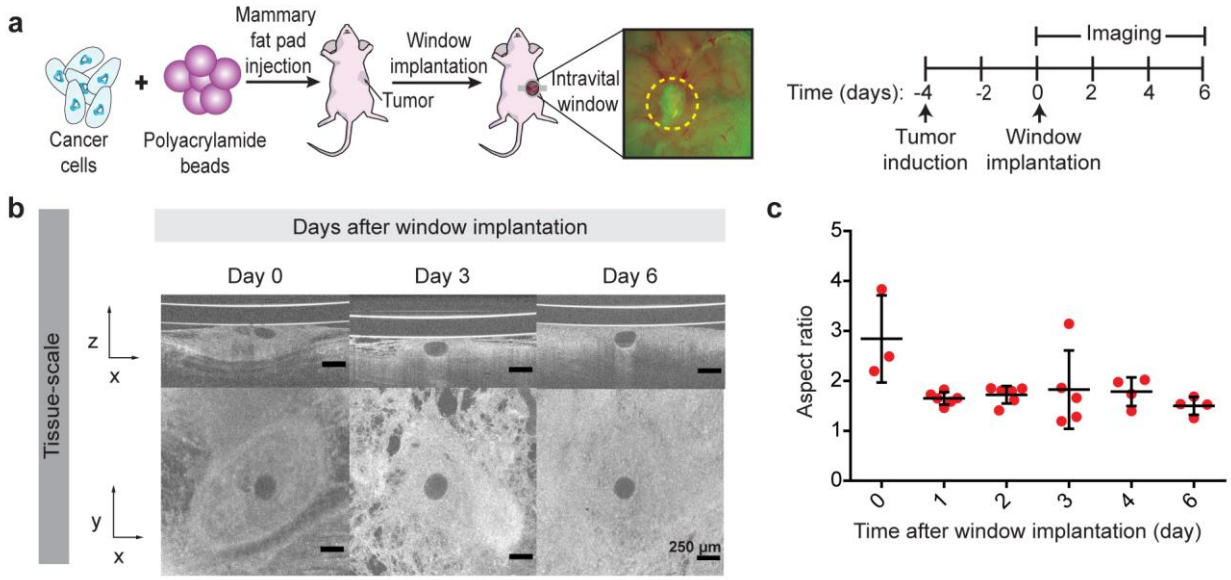

Figure S4| Window implantation after tumor growth causes artificial compression. a, Methodology and timeline for tumor induction. The outlined image was taken using a fluorescent stereomicroscope. **b,** After demonstrating that window implantation after tumor formation applies artificial compression which relaxes over 6 days, we switched to window implantation before the tumor induction. We demonstrated that window implantation before the tumor induction does not alter the solid stress level (**Fig. 2h**). The XZ and XY views of bead (E= 1.3 ± 0.13 kPa) in tumor at days 0, 3, and 6, captured with OCT. **c,** Aspect ratios of polyacrylamide beads over time (mean ± STD, n=3-6 beads).

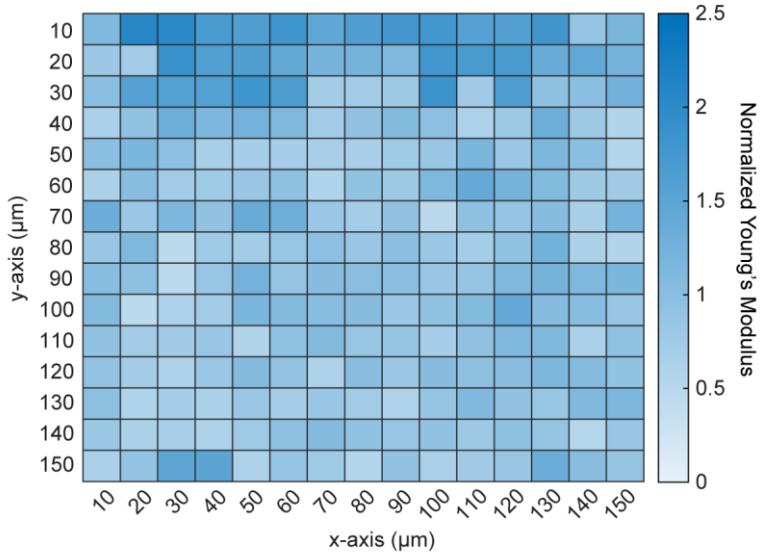

Figure S5| Mapping of the Young's modulus in polyacrylamide. AFM mapping of a bulk polyacrylamide hydrogel shows that 87.5% of Young's modulus values fall between a factor of 0.5 and 1.5 of the average Young's modulus. The map of Young's moduli is normalized by the mean Young's modulus.

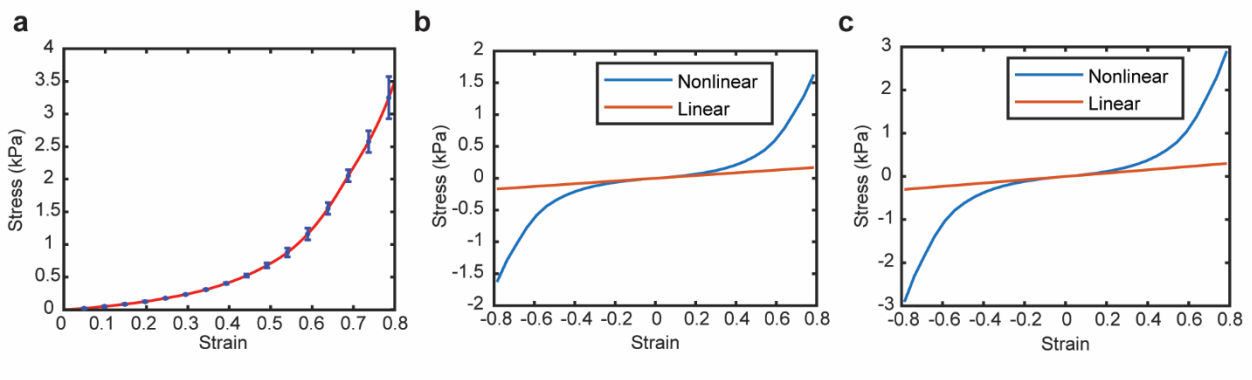

Figure S6| Nonlinear behavior of polyacrylamide hydrogels. a, Axial compression curve of polyacrylamide hydrogel. **b,** fitting nonlinear curve to cellular-scale bead Young's modulus of 215 Pa. **c,** fitting nonlinear curve to tissue scale bead Young's modulus of 383 Pa.

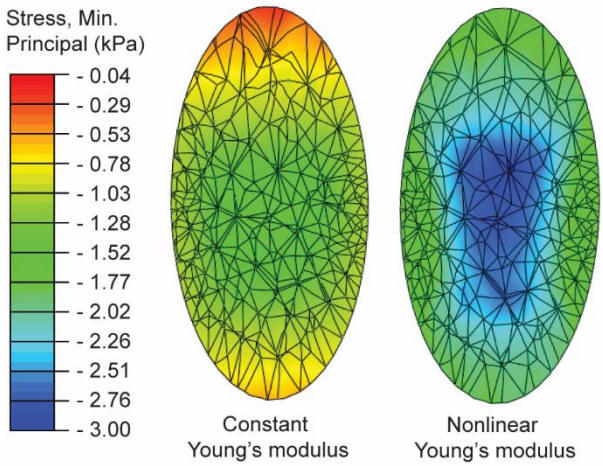

Figure S7| Comparison of constant Young's modulus (linear stress/strain) and nonlinear Young's modulus using hyperelastic FEM. Cross-section of tissue-scale FE model. The average of the absolute principal stresses is 752 Pa when constant Young's modulus is used, compared to 1475 Pa when nonlinear Young's modulus is used.

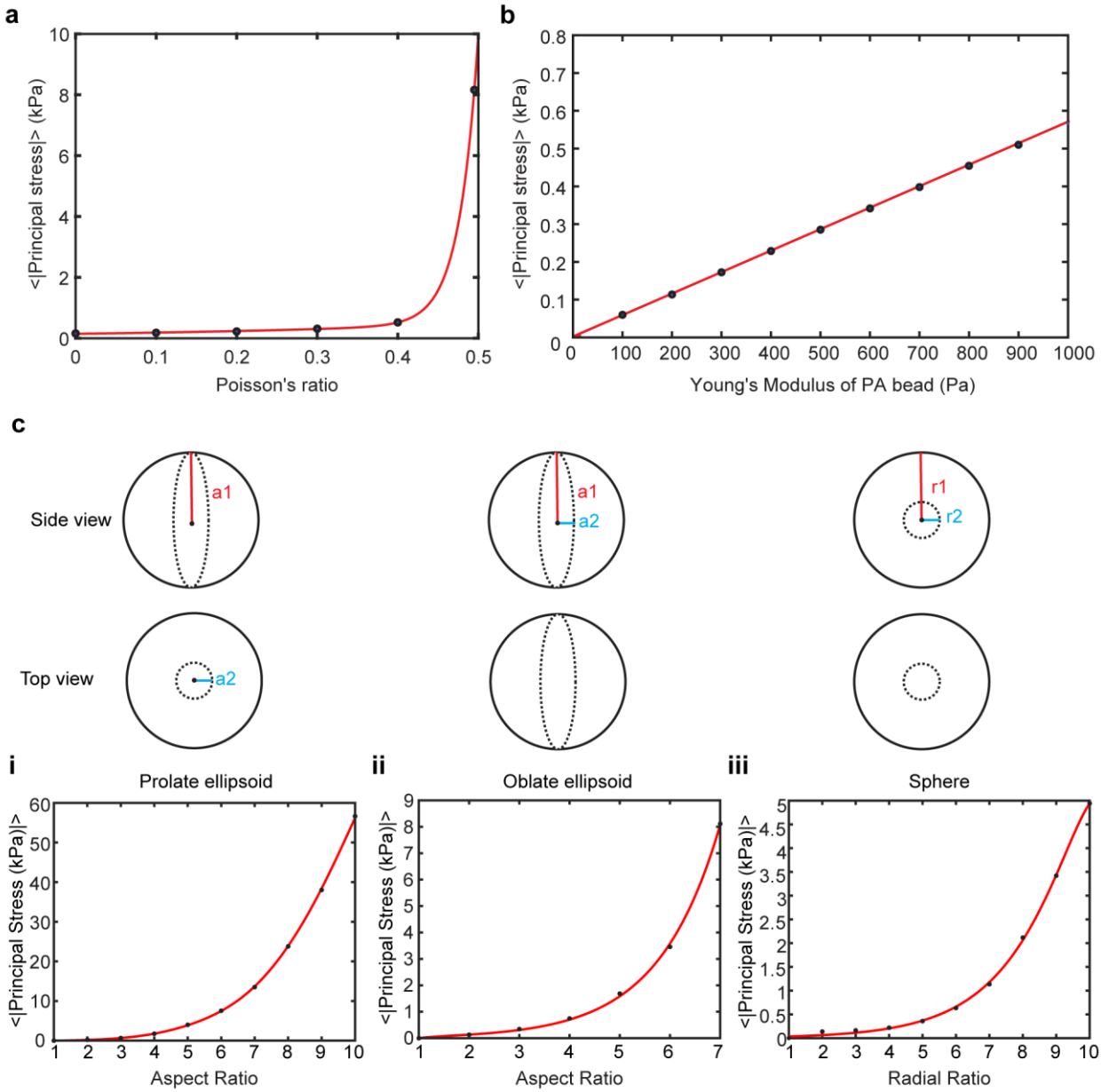

Figure S8| Parametric study of the effect of Poisson's ratio, Young's modulus, and anisotropic and isotropic deformation geometries on FEM stress values. a, The Poisson's ratio was parametrically altered between 0 (ideal compressible material) and 0.5 (ideal incompressible material) in a finite element model and resulted in exponentially increasing average max absolute principal stress values as Poisson's ratio approaches 0.5. **b,** The Young's modulus was altered between 0 and 1000 Pa. Young's modulus has a positive linear relationship with the average absolute minimum principal stress. **c,** Stress increases with increasing aspect ratio (a1:a2) for **(i)** prolate and **(ii)** oblate ellipsoids and with radial ratio (r1:r2) for **(iii)** isotropic deformations which result in a sphere. The spheres in solid black outline represent the original spherical geometry of the undeformed bead and the dotted lines represent the deformed geometry. Aspect ratios and radial ratios were varied from 1 to 10 for all geometries. The FEM for oblate ellipsoids which had aspect ratios above 7 did not converge and therefore the values are not reported.

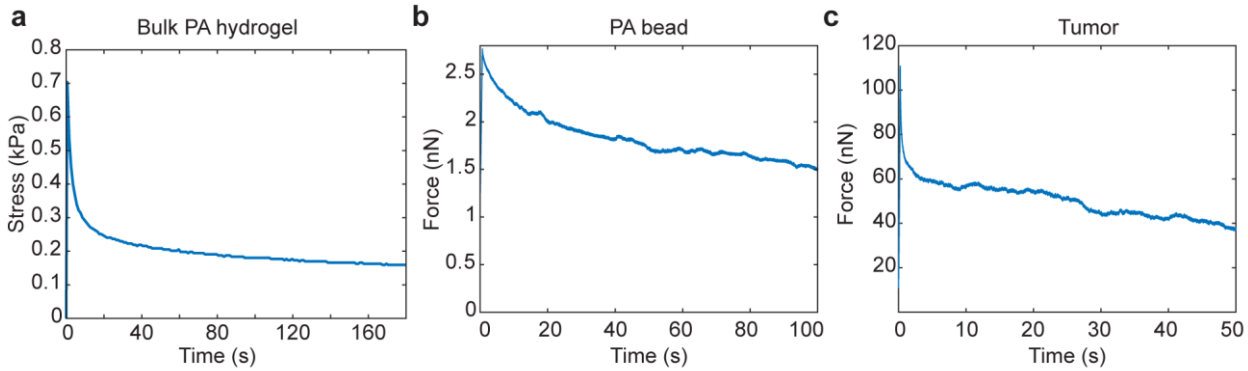

Figure S9| Stress relaxation time constants of polyacrylamide beads and tumors are on similar time scales. The indentation curves of a bulk polyacrylamide hydrogel, a tissue-scale PA beads and an E0771-H2B-dendra2 tumor were calculating using the equation, $\sigma = \sigma_0 * e^{-(t_0 - t)/\tau}$, where τ is the stress relaxation time constant. **a,** The stress relaxation time constant is 73 seconds for bulk polyacrylamide hydrogel, **b,** 17 seconds for tissue-scale PA beads, and **c,**15 seconds for E0771-H2B-dendra2 tumors.

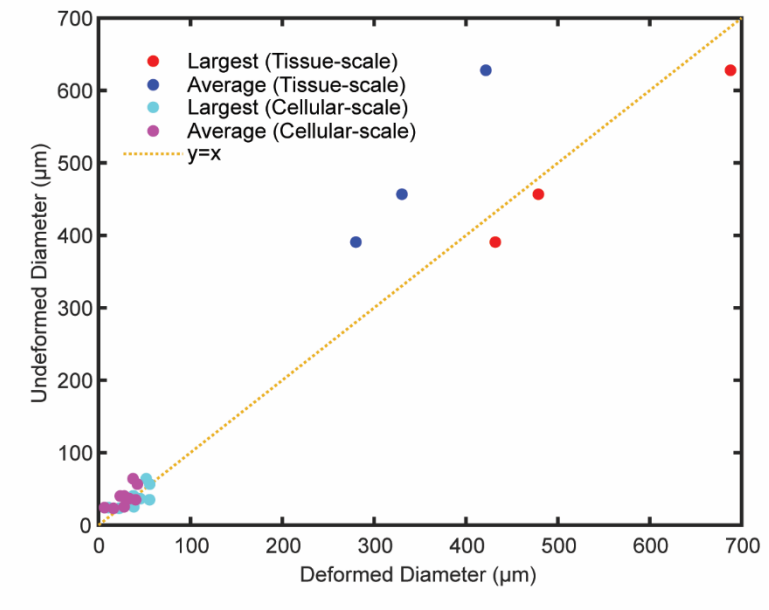

Figure S10| Original diameter selection for bead analysis. To determine the closest approximation for the undeformed diameter of beads, deformed beads in spheroids were relaxed via enzymatic dissociation of the spheroid with trypsin. The values for the undeformed diameter of each deformed bead was determined via enzymatic dissociation of the spheroid to relax the deformed beads. Assuming the undeformed diameter is the true original diameter, y=x is the ideal prediction line. The R^2 value is 0.692 when using the average deformed diameter as the original diameter compared to an R^2 value of 0.988 when using the largest deformed diameter as the original diameter. The largest diameter of the deformed bead is the closest estimate for the diameter of the undeformed bead. (n=7 cellular-scale beads, 3 tissue-scale beads)

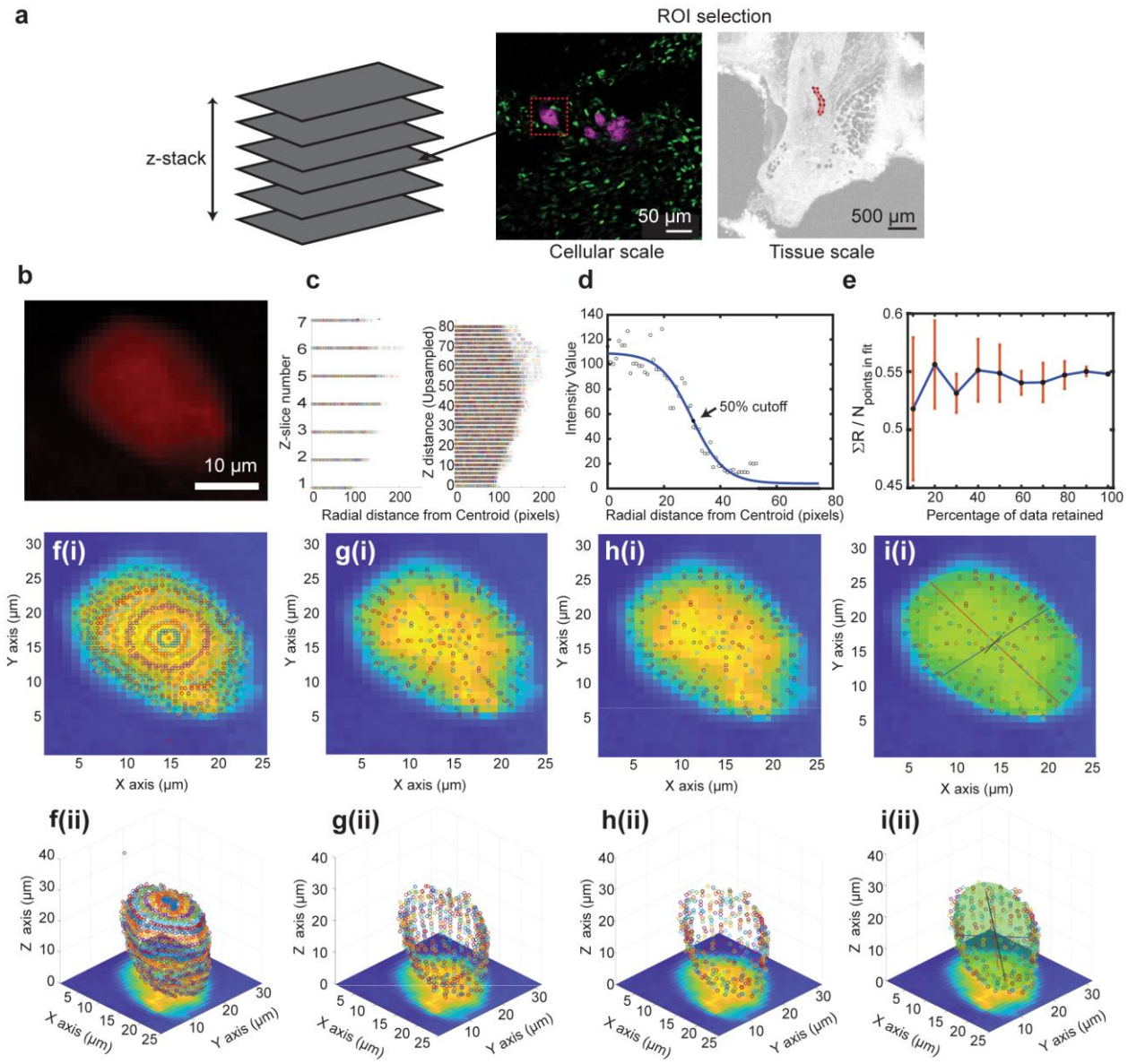

Figure S11| Image segmentation and ellipsoid fitting. a, ROI selection for cellular and tissue scales (cellular scale: beads (magenta), cancer cells (green), tissue scale: bead (outlined in red)). **b,** Bead of interest from a sample image. **c,** The image is up-sampled in the z-dimension to have a similar apparent resolution as in the x- and y-dimensions while preserving spatial information, as evident in the pixel projections along the radial distance from the centroid. **d,** From the centroid of the stack, radial paths are traced out through θ and ϕ values with gradual increments in ray length r. A sigmoidal function is fit to the data and the 50% intensity value is taken to represent the boundary of the bead. **e,** After a reduction in data by θ and ϕ values, a final 60% of data is kept, as this value balanced a low residual distance between ellipsoid fit and data points (y-axis: sum of residuals normalized by number of points in the fit) and a reliable performance range (mean ± STD, n=10). **f-i (i),** Through the data down-sampling process the point-cloud accurately captures the shape of the bead, as shown projected over the central plane. **f-i (ii)**, From the final ellipsoid fit, 3 principal axes lengths can be calculated.

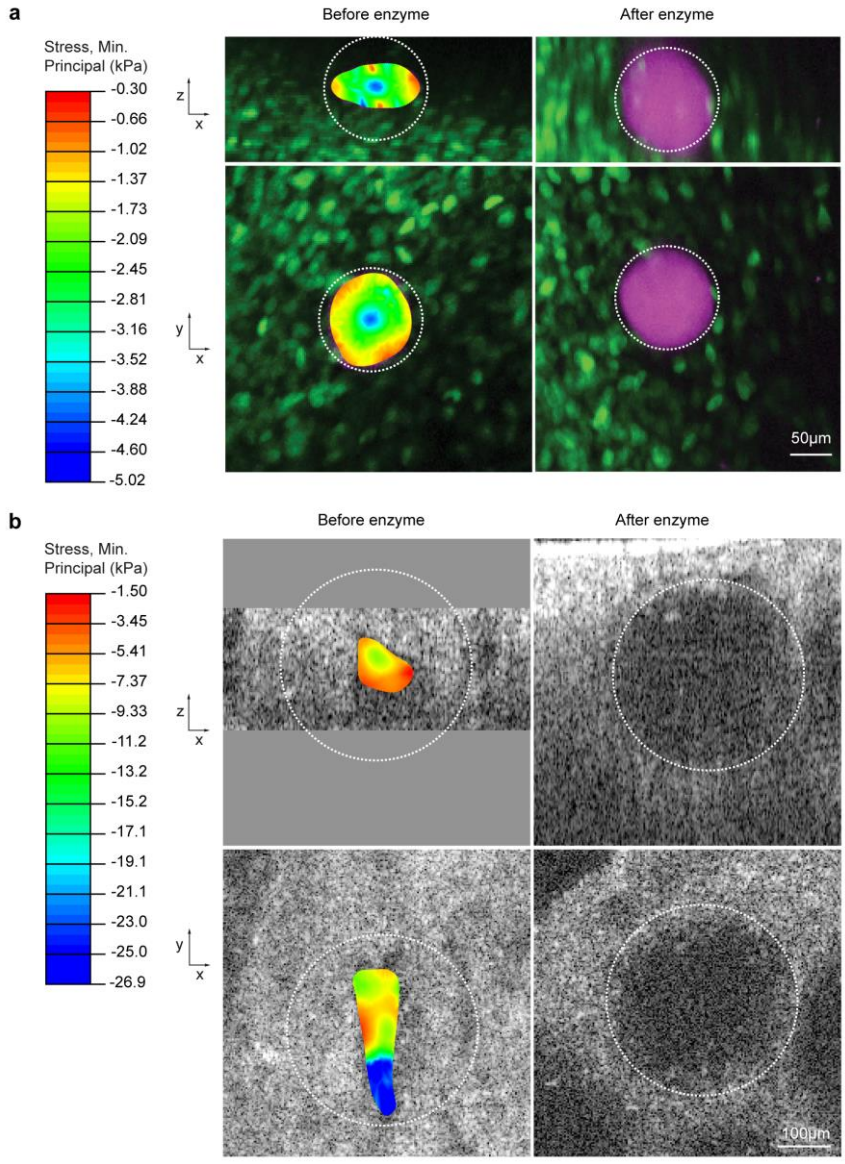

Figure S12| Isotropic PA bead deformation at cellular and tissue scale. By enzymatically dissociating tissue to relax bead deformation, our method is able to measuring total stress, including isotropic and anisotropic deformation in the bead at the **a,** cellular and **b,** tissue scales.

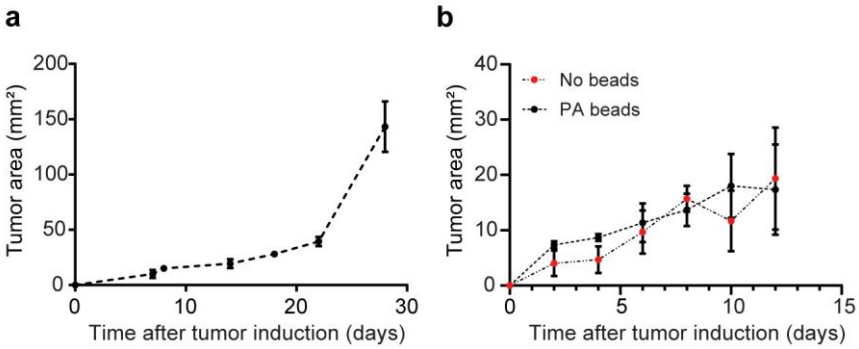

Figure S13| Tumor growth is not altered by the presence of beads. a, Tumor growth of MCa-M3C-H2B-dendra2 without PA beads with cells injected under the skin into the mammary fat pad (mean ± SEM, N=5 mice)**. b,** Tumor growth of E0771-H2B-dendra2 with and without PA beads. Tumors with and without PA beads have similar growth rates (mean ± SEM, N=3 mice)

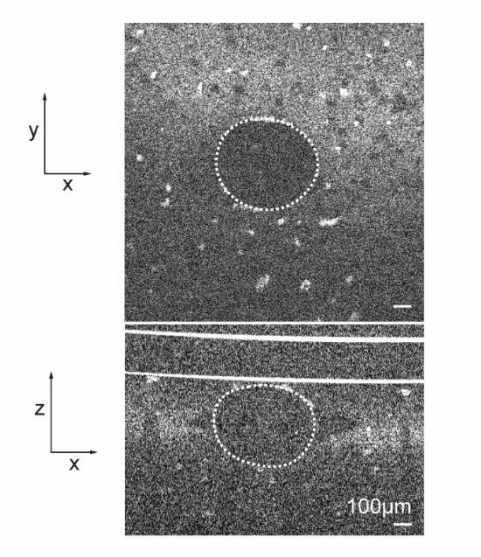

Figure S14| Embedding polyacrylamide beads and MCa-M3C-H2B-dendra2 cancer cells in Matrigel for day 0 imaging at tissue scale. Using polyacrylamide beads and MCa-M3C-H2B-dendra2 cancer cells embedded in Matrigel, beads can be visualized at the tissue-scale in vivo for longitudinal determination of solid stress from day 0

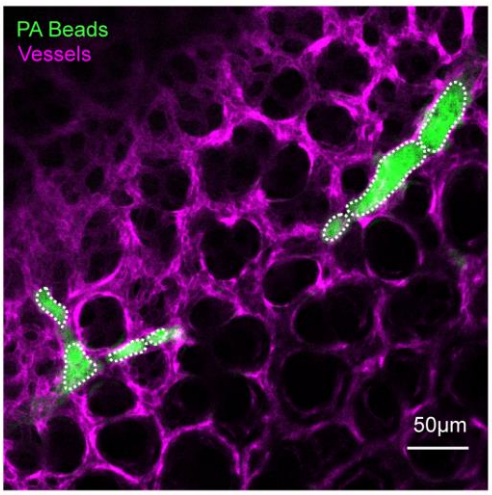

Figure S15| Delivery of tissue-scale beads tail-vein cause clogging of lung vasculature. The measurement of tissue-scale stresses in the lung is not feasible due to the stoppage of blood flow by tissue-scale beads in arterioles.

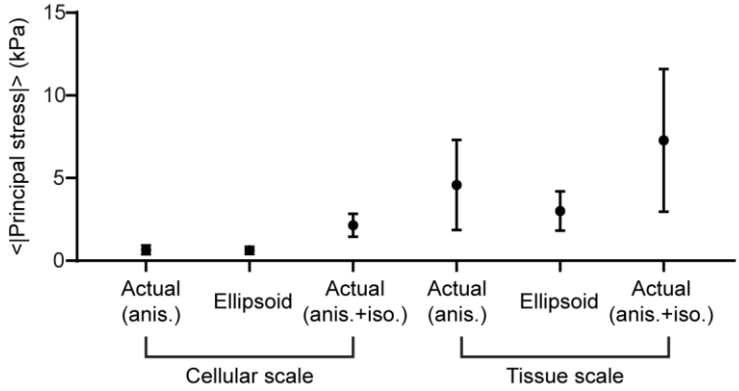

Figure S16| Comparison of stress from finite element modeling of the original deformed geometry deformation vs the ellipsoid fit. The reported stress is the mean ± STD of one bead each at the cellular and tissue scale. At the cellular scale, for the original deformed bead geometry with only anisotropic stresses, the stress is 0.662 ± 0.270 kPa; for the ellipsoid fit the stress is 0.625 ± 0.215 kPa; for the original deformed bead geometry with total stress (anisotropic and isotropic) the stress is 2.15 ± 0.695 kPa. At the tissue scale, for the original deformed bead geometry with only anisotropic stresses, the stress is 4.58 ± 2.73 kPa; for the ellipsoid fit the stress is 3 .01 ± 1.19 kPa; for the original deformed bead geometry with total stress, the stress is 7.28 ± 4.31 kPa. The ellipsoid fit is more appropriate for determining stresses in purely anisotropic cases and underestimates stress in cases with both anisotropic and isotropic deformation.

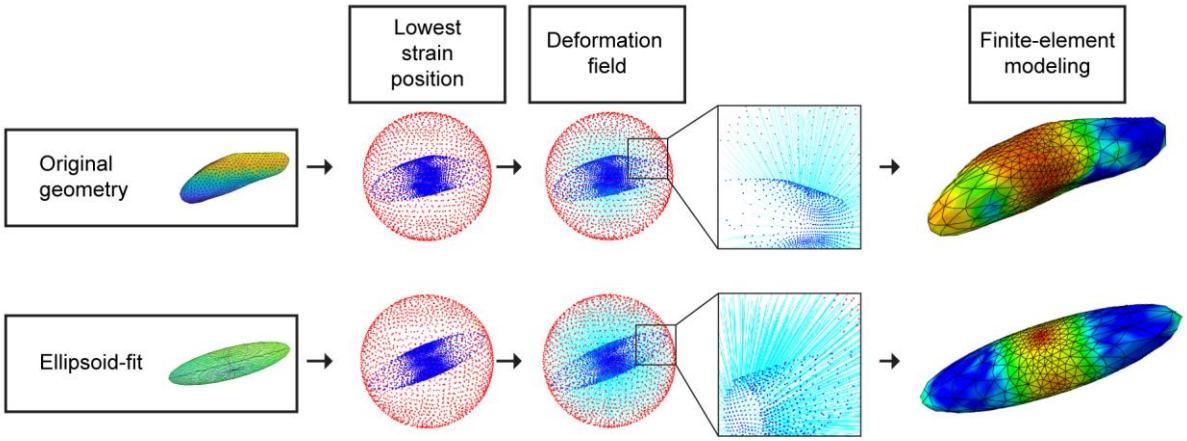

Figure S17| Mathematical modeling of deformed beads. Using either the original deformed geometry or the ellipsoid fit, the position of the deformed bead where the lowest strain occurs is used to calculate the deformation field from the surface of the deformed bead to the original undeformed bead. Then, finite element modeling is used to calculate the 3-D stresses within the deformed PA bead.

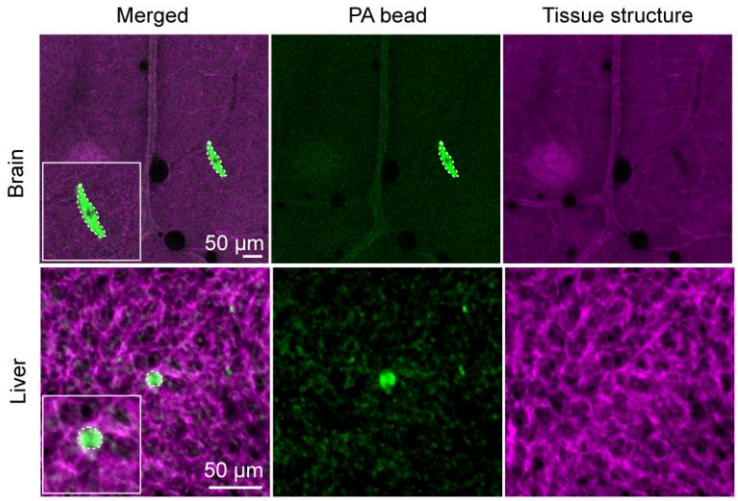

Figure S18| PA beads be delivered to the liver and brain of mTmG mice. PA beads can be delivered to both liver and brain to measure solid stress.

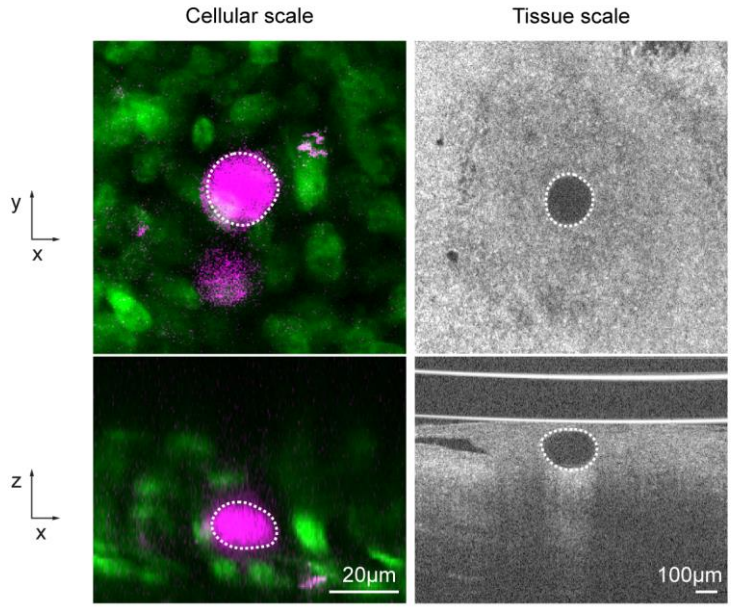

Figure S19| Intermediate Young's modulus. While optimizing for the Young's modulus of PA beads in order to achieve dynamic range in measuring solid stress, PA beads with intermediate Young's moduli were used at the cellular (0.77 ± 0.16 kPa) and tissue scales (1.3 ± 0.13 kPa).